The Astrophysical Journal, 634:476–494, 2005 November 20

HIGH-MASS CLOUD CORES IN THE η CARINAE GIANT MOLECULAR CLOUD

Yoshinori Yonekura,[1] Shin'ichiro Asayama,[1,2] Kimihiro Kimura,[1] Hideo Ogawa,[1] Yoko Kanai,[3] Nobuyuki Yamaguchi,[2,3] Peter J. Barnes,[4,5] and Yasuo Fukui[3]

Received 2004 October 26; accepted 2005 August 2

ABSTRACT

We carried out an unbiased survey for massive dense cores in the giant molecular cloud associated with η Carinae with the NANTEN telescope in the ^{12}CO, ^{13}CO, and C^{18}O $J = 1-0$ emission lines. We identified 15 C^{18}O cores, whose typical line width $\Delta V_{\rm comp}$, radius r, mass M, column density $N(\rm H_2)$, and average number density $n(\rm H_2)$ were 3.3 km s^{-1}, 2.2 pc, 2.6×10^3 $M_\odot$, 1.3×10^{22} cm^{-2}, and 1.2×10^3 cm^{-3}, respectively. Two of the 15 cores are associated with *IRAS* point sources whose luminosities are larger than 10^4 $L_\odot$, which indicates that massive star formation is occurring within these cores. Five cores, including the two with *IRAS* sources, are associated with *MSX* point sources. We detected H^{13}CO$^+$ ($J = 1-0$) emission toward four C^{18}O cores, two of which are associated with *IRAS* and *MSX* point sources; another one is associated only with an *MSX* point source, and the other is associated with neither *IRAS* nor *MSX* point sources. The core with neither *IRAS* nor *MSX* point sources shows the presence of a bipolar molecular outflow in ^{12}CO ($J = 2-1$), which indicates that star formation is also occurring in the core, and the other three of the four H^{13}CO$^+$ detections show winglike emission. In total, 6 C^{18}O cores out of 15 (=40%) have experienced star formation, and at least 2 of 15 (=13%) are massive star–forming cores in the η Car GMC. We found that massive star formation occurs preferentially in cores with larger $N(\rm H_2)$, M, and $n(\rm H_2)$ and a smaller ratio of $M_{\rm vir}/M$. We also found that the cores in the η Car GMC are characterized by large ΔV and $M_{\rm vir}/M$ on average compared to the cores in other GMCs observed with the same telescope. These properties of the cores may account for the fact that as much as 60%–87% of the cores do not show any signs of massive star formation. We investigated the origin of a large amount of turbulence in the η Car GMC. We found that turbulence injection from stellar winds, molecular outflows, and supernova remnants that originated from stars formed within the GMC are not enough to explain the existing turbulence. We propose the possibility that the large turbulence was preexisting when the GMC was formed and is now dissipating. Mechanisms such as multiple supernova explosions in the Carina flare supershell may have contributed to form a GMC with a large amount of turbulence.

Subject headings: ISM: clouds — ISM: individual (η Carinae GMC) — ISM: molecules — radio lines: ISM — stars: formation

1. INTRODUCTION

It is well established that massive stars form in dense cores within giant molecular clouds (GMCs), while low-mass stars form in both dark clouds and GMCs. The formation process of an isolated low-mass star is fairly well understood: the gravitational collapse of a molecular cloud into a protostellar core and the subsequent accretion via a circumstellar disk surrounded by an infalling envelope (e.g., Shu et al. 1987 and references therein), followed by the dissipation of momentum into its surroundings through molecular outflows (Lada 1985; Fukui et al. 1986, 1993; Fukui 1989 and references therein). The current paradigm is now being tested by observations, and it has become clear that some modifications to the details of protostellar formation are needed (e.g., André et al. 1993; Onishi et al. 1996, 1998; Evans 1999 and references therein).

Concerning massive star formation, an empirical scenario of the later stages of the massive star formation process has been presented (e.g., Kurtz et al. 2000 and references therein); dense ($\sim10^7$ cm^{-3}), compact ($\lesssim$0.1 pc), and hot ($\gtrsim$100 K) regions called hot cores are formed in GMCs, then the UV radiation from newly formed stars within hot cores ionizes the surrounding material to produce ultracompact H II regions (UCHIIs), and finally the central stars become visible, such as the Trapezium cluster in Orion. On the other hand, evolution before the formation of hot cores remains unclear, although some attempts to detect sources at the earliest stages of massive star formation have been made; surveys toward *IRAS* (*Infrared Astronomical Satellite*) point sources and maser sources (e.g., Beuther et al. 2002a; Mueller et al. 2002; Sridharan et al. 2002; Shirley et al. 2003) have revealed the presence of the dense, compact, and massive cores (density $\gtrsim10^6$ cm^{-3}, temperature $\gtrsim$100 K, luminosity $\gtrsim10^4$ $L_\odot$) sometimes called high-mass protostellar objects (HMPOs; Sridharan et al. 2002), some of which are not accompanied by UCHIIs. Although sources without UCHIIs may be younger than the rest, the presence of *IRAS* point sources and maser sources themselves strongly indicates that stars are already formed within HMPOs. It is quite natural to suppose that dense, compact, massive, *starless* cores (density $\sim10^6$ cm^{-3}, size $\lesssim$1.0 pc, mass $\gtrsim10^3$ $M_\odot$) are the precursors of the HMPOs and hot cores (e.g., Evans et al. 2002). Systematic studies of these massive starless cores had not been carried out until recently, due to the difficulty in selecting targets from the existing database. It is to be noted that large-scale surveys for possible candidates for massive starless cores (density $\sim10^4$ cm^{-3}) have already been

[1] Department of Physical Science, Osaka Prefecture University, 1-1 Gakuen-cho, Sakai, Osaka 599-8531, Japan; yonekura@p.s.osakafu-u.ac.jp.
[2] Current address: National Astronomical Observatory of Japan, 2-21-1 Osawa, Mitaka, Tokyo 181-8588, Japan.
[3] Department of Astrophysics, Nagoya University, Furo-cho, Chikusa-ku, Nagoya 464-8602, Japan.
[4] School of Physics A28, University of Sydney, NSW 2006, Australia.
[5] School of Physics OMB, University of New South Wales, NSW 2052, Australia.

made; e.g., Lada et al. (1991) surveyed the L1630 cloud (Orion B) in CS ($J = 2-1$). The importance of the study of starless cores has been revealed in a series of unbiased surveys for dense cores in low-mass star–forming regions, especially from the viewpoint of setting observational constraints on the evolutional timescales of the theoretical model (Onishi et al. 1996, 1998; Tachihara et al. 2002). The same is expected for the massive star–forming regions, and thus unbiased surveys for massive dense cores in massive star–forming regions are also crucial.

One of the most important tasks in the study of massive star formation at the moment is to identify massive dense cores that have not yet experienced massive star formation but are capable of future massive star formation. High-resolution observations of these cores will give observational constraints on the initial phases of the evolutional model of a massive star; massive stars are formed by direct accretion onto a central protostar through an accretion disk (e.g., McKee & Tan 2003), which is a simple extension of low-mass star formation, or by collisions of intermediate-mass protostars within a young cluster (e.g., Bonnell et al. 1998). Moreover, such observations are the only method of revealing the initial conditions of massive star–forming cores, since the properties of the cores change rapidly soon after the formation of massive stars due to strong UV radiation and stellar winds. Surveys for hot cores and HMPOs toward *IRAS* point sources and maser sources are, however, biased toward regions that have experienced star formation, and thus it is not possible to obtain information on the initial conditions of the massive star–forming cores. Therefore, studies of dense cores that have not yet experienced massive star formation are awaited. Unbiased surveys for massive dense cores over entire GMCs in molecular lines, as well as in the far-infrared and (sub-) millimeter continuum, may be the most effective methods of searching for massive starless cores that are capable of future massive star formation. Far-IR and submillimeter/millimeter continuum observations are best suited to detect radiation from the dust in starless cores, since the radiation from cold dust ($T \lesssim 20$ K) peaks at far-IR ($\gtrsim 150$ μm) wavelengths with a gradual decrease toward longer wavelengths. The recent development of sensitive instruments, such as bolometer array receivers, makes (sub-) millimeter continuum observations more effective for carrying out a large-scale survey for massive dense cores. An unbiased survey of entire GMCs with (sub-) millimeter continuum has not yet been made, but several surveys in small fields surrounding *IRAS* point sources are now in progress for the purpose of detecting massive dense cores located near the *IRAS* point sources. Thus far, regions of $\sim 10' \times 10'$ around $\sim$200 *IRAS* point sources have been observed at a resolution of $8''$–$24''$ (Forbrich et al. 2004; Faúndez et al. 2004). Based on these surveys, a few massive dense cold cores without mid-IR (*MSX* [*Midcourse Space Experiment*]) and far-IR (*IRAS*) counterparts have been found (Forbrich et al. 2004; Garay et al. 2004). Molecular line observations have the invaluable merit of drawing kinematic information from the cores, which is impossible in continuum observations. The empirical relation between the luminosity of the forming star and the line width of the parent dense core has been found by many authors from observations in NH_3 (e.g., Stacy et al. 1988; Wouterloot et al. 1988; Myers et al. 1991; Harju et al. 1993; Ladd et al. 1994; Jijina et al. 1999), as well as in $C^{18}O$ (e.g., Saito et al. 2001), which makes molecular line observations still more important.

We, the NANTEN group, are now conducting unbiased surveys for dense cores in the $C^{18}O$ ($J = 1-0$) line with the NANTEN 4 m millimeter telescope. Tachihara et al. (2002) compiled a sample of 174 $C^{18}O$ dense cores in low-mass star–forming regions of Taurus (Onishi et al. 1996, 1998), L1333 (Obayashi et al. 1998), Ophiuchus North (Nozawa et al. 1991), ρ Oph (Tachihara et al. 2000), Chamaeleon (Mizuno et al. 1999), Lupus (Hara et al. 1999), Corona Australis (Yonekura et al. 1999), the Pipe Nebula (Onishi et al. 1999), and the Southern Coalsack (Kato et al. 1999), including intermediate-mass cluster–forming regions such as ρ Oph, Cha I, R CrA, and Lup 3, and found that cores with active star formation tend to have larger column density, number density, and mass and tend to be gravitationally more bound. Observations toward massive star–forming regions are also in progress; we have detected 112 cores so far in the unbiased surveys for dense cores in GMCs such as Orion A, Orion B, Cep OB3, Vela, S35/S37, and Centaurus (Yu et al. 1996; Nagahama 1997; Yamaguchi et al. 1999a; Saito et al. 1999, 2001; Aoyama et al. 2001). The beam size of the NANTEN telescope, $2'.7$ ($\sim$0.3 pc at the distance of the nearest GMC, Orion B, $D = 400$ pc), is not necessarily sufficient to resolve massive starless cores. However, it is still meaningful to select *candidates* for massive starless cores (density $\sim 10^4$ cm^{-3}, size around a few parsecs, mass at least a few $\times 10^3$ $M_\odot$, which are estimated from the physical parameters of massive starless cores), which can be traced by $C^{18}O$ ($J = 1-0$) observations with NANTEN, since only a few massive starless cores have been identified so far. In this paper, we report the results of an unbiased survey for dense cores in the GMC associated with the η Carinae nebula (the η Car GMC hereafter), with the aim of obtaining samples of massive starless core candidates that are possible sites for future massive star formation.

The η Car GMC has been one of the most active star-forming regions in the Galaxy at least until the formation of the youngest stellar cluster associated with the GMC ($\sim$3 Myr ago; e.g., Feinstein 1995). Eight stellar clusters (Trumpler 14, 15, 16, Collinder 228, Bochum 10, 11, NGC 3293, and NGC 3324; hereafter we abbreviate Trumpler 14 and Trumpler 16 as Tr 14 and Tr 16, respectively) are associated with the GMC, which contains more than 64 O-type stars including one of the most massive stars, η Car (Feinstein 1995). When we estimate the star formation activity from the richness of the clusters by counting the number of the most massive stars (e.g., stars with spectral type O3) since the total number of the cluster members cannot be counted, the η Car GMC (with five O3 stars) is estimated to be the second most active star-forming region after NGC 3603 with six O3 stars (Maíz-Apellániz et al. 2004). Its proximity to the Sun ($D \sim 2.5$ kpc for the η Car GMC compared to 6.9 kpc for NGC 3603) makes the η Car GMC the best site for the detailed study of massive star formation because much higher spatial resolution can be achieved. There is a possibility that active star-forming regions, such as W49, where more than 100 O-type stars have been found in infrared observations (Alves & Homeier 2003), are hidden in the Galactic plane due to heavy foreground extinction. However, it is natural to think that regions with heavy foreground extinction are located distant from the Sun (11.4 kpc in the case of W49), and thus the η Car GMC still remains advantageous. It is to be noted that the well-studied massive star–forming region, the Orion region, is a much smaller system, containing only a single O4–6 star (Maíz-Apellániz et al. 2004).

Several observations have been made so far covering the entire η Car GMC with moderate spatial resolution. Grabelsky et al. (1987, 1988) observed the whole η Car GMC (3×2 deg^2) in the ^{12}CO ($J = 1-0$) line with an $8'.8$ beam and revealed the existence of a string of CO clouds between $l = 284^\circ.7$ and 289° with a total mass of 6.7×10^5 $M_\odot$. Zhang et al. (2001b) made submillimeter observations in ^{12}CO ($J = 4-3$) and atomic carbon [C I] $^3P_1$–$^3P_0$ with a $3'$ beam and found that these two emissions and ^{12}CO ($J = 1-0$) are approximately coextensive and

that the excitation temperature is higher (~50 K near η Car and ~20 K in clouds farther from η Car) than that in dark clouds. High-resolution observations at a resolution of ~20″–40″ were made toward some selected clouds near η Car. There are two main CO emission regions near η Car: the northern and southern clouds (de Graauw et al. 1981; Brooks et al. 1998). The northern cloud lies surrounding the cluster Tr 14 (~7 pc northwest of η Car). Brooks et al. (2003) observed the northern cloud and found that the cloud consists of four main CO clouds with masses in the range 40–500 $M_\odot$, two of which are gravitationally bound with density exceeding 10^5 cm^{-3}. They proposed that these clouds are exposed to a radiation field originating mainly from the most massive stars in Tr 14. The southern cloud is located adjacent to the cluster Tr 16, which includes η Car. Megeath et al. (1996) found a gravitationally bound cloud with a mass of 70 $M_\odot$ and that a cold *IRAS* point source with luminosity ~10^4 $L_\odot$ is associated with the cloud. They concluded that star formation is ongoing at the interface between the cloud and the cluster Tr 16, which is triggered by radiation-driven shocks. Between the northern and the southern clouds, the distribution of the molecular gas is patchy due to dissociation by the strong UV radiation and stellar winds from nearby massive stars in Tr 16 (Cox & Bronfman 1995). They also found that the typical mass of the clouds is ~10 $M_\odot$ and that the clouds are not gravitationally bound. Recently, Rathborne et al. (2004) studied the region called the giant pillar (Smith et al. 2000), ~0.°5 south of η Car. Since the distance from the clusters is larger than that of the northern and southern clouds, and since the giant pillar is located behind the southern cloud, the influence of the UV radiation and stellar winds from the clusters may be smaller and the photodissociation may take longer than in the northern and southern clouds. From CO $J = 2-1$ observations toward four mid-IR sources identified by Smith et al. (2000) using mid-infrared data obtained by *MSX*, they found that these sources are also influenced by the radiation from clusters Tr 14 and Tr 16. The mass of the associated clouds ranges from 10 to 45 $M_\odot$, and they are probably not gravitationally bound. They also found 12 candidates for massive young stellar objects and UCHIIs from the mid-IR data. These studies revealed that star formation is still ongoing in the η Car GMC under the strong influence of the most massive stars in clusters, in regions of at least 1.5×2 deg^2 in the vicinity of η Car.

Here we report the results of an unbiased survey for dense cores in the entire η Car GMC. The purpose of the present study is to obtain a sample of massive starless core candidates that are possible sites for future massive star formation. With moderate spatial resolution, 2.′7, our observation covered the entire η Car GMC (3×2 deg^2) including regions farther from η Car, such as the western part of the η Car GMC around the H II region Gum 31 and the southernmost part of the η Car GMC, where no previous observations had been made except coarse large-scale surveys. Observations were made in C^{18}O ($J = 1-0$), as well as in ^{12}CO and ^{13}CO, with NANTEN. We also made high-resolution observations in H^{13}CO$^+$ ($J = 1-0$) with the Mopra 22 m millimeter telescope and searched for molecular outflows in ^{12}CO ($J = 2-1$) toward some selected dense cores with the Atacama Submillimeter Telescope Experiment (ASTE) 10 m submillimeter telescope. Of the 15 C^{18}O cores detected in this survey, two are ongoing massive star–forming cores associated with luminous infrared sources and another four are possibly less massive star–forming cores, and thus as many as 9–13 cores that have not experienced massive star formation are detected in this survey. We present the physical properties of the dense cores and compare the star formation activity with them. We also compare the properties of the C^{18}O cores with those in other massive star–forming regions, such as Orion, Cepheus, Vela, S35, and Centaurus, in order to study the characteristics of the η Car GMC.

2. OBSERVATIONS

2.1. *Large-Scale Observations of* CO *Gas and the Search for High-Mass Cores*

Observations of the $J = 1-0$ transitions of ^{12}CO, ^{13}CO, and C^{18}O were made with the NANTEN 4 m telescope of Nagoya University at Las Campanas Observatory of the Carnegie Institution of Washington (Fukui et al. 1991; Fukui & Sakakibara 1992; Fukui & Yonekura 1998). The half-power beamwidth of the telescope was 2.′7 at 110 GHz and 2.′6 at 115 GHz, corresponding to ~2 pc for the distance of the η Car GMC, 2.5 kpc. The 4 K cooled SIS mixer receiver provided a typical system temperature of ~140 K (single-sideband [SSB]) at 110 GHz and ~200 K (SSB) at 115 GHz, including the atmosphere toward the zenith (Ogawa et al. 1990). The spectrometer was an acousto-optical spectrometer with a total bandwidth of 40 MHz divided into 2048 channels. The effective spectral resolution was 40 kHz, corresponding to a velocity resolution of 0.11 km s^{-1} at 110 GHz.

The ^{12}CO data were obtained from 1998 May to July and in 1999 March. Most of the region was observed by using a position-switching technique with a grid spacing of 2′, and the rest with a 4′ grid. The total integration time and the typical rms noise of the data at a velocity resolution of 0.1 km s^{-1} were ~5 s and $\Delta T_{\rm rms} \sim$ 1.0 K, respectively. In ^{13}CO, observations were made from 1999 January to March with a 4′ grid by using a position-switching technique. The total integration time per point was ~5 s, and the typical rms noise of the data was $\Delta T_{\rm rms} \sim 0.4$ K at a velocity resolution of 0.1 km s^{-1}. C^{18}O observations were made in three periods from 1998 July to August, in 1999 March, and from 2003 August to October. The data were obtained with a grid spacing of 2′. A frequency-switching technique was used with a switching interval of 13 MHz in 1998 and 1999, whereas a position-switching technique was used in 2003. The total integration time per point was ~90 s, and the typical rms noise of the data was $\Delta T_{\rm rms} \sim$ 0.1 K at a velocity resolution of 0.1 km s^{-1}.

For the calibration of the spectral line intensity, a room-temperature chopper wheel was employed. The absolute-intensity calibration was made by observing Ori KL ($\alpha_{1950} = 5^{\rm h}32^{\rm m}47\overset{\rm s}{.}0$, $\delta_{1950} = -5^\circ 24' 21''$) and ρ Oph East ($\alpha_{1950} = 16^{\rm h}29^{\rm m}20\overset{\rm s}{.}9$, $\delta_{1950} = -24^\circ 22' 13''$). The peak radiation temperatures, T_R^*, are assumed to be $T_R^*(^{12}\mathrm{CO}, \mathrm{Ori\ KL}) = 65$ K (Ulich & Haas 1976; Kutner & Ulich 1981; Levreault 1988), $T_R^*(^{13}\mathrm{CO}, \mathrm{Ori\ KL}) = 10$ K (Mizuno et al. 1995), and $T_R^*(\mathrm{C}^{18}\mathrm{O}, \rho\ \mathrm{Oph\ East}) = 4.4$ K. The last value is consistent with the assumption that $T_R^*(\mathrm{C}^{18}\mathrm{O}, \mathrm{TMC\ 1}[\alpha_{1950} = 4^{\rm h}38^{\rm m}42\overset{\rm s}{.}0, \delta_{1950} = 25^\circ 35' 45'']) = 2.0$ K (Onishi et al. 1996), which has been established by the long-term monitoring of standard sources done at the NANTEN telescope. The pointing accuracy was measured to be better than 20″, as checked by optical observations of stars with a CCD camera attached to the telescope, as well as by radio observations of Jupiter, Venus, and the edge of the Sun.

2.2. *Detailed Observations for High-Density Regions*

Observations of the $J = 1-0$ transition of H^{13}CO$^+$ were made with Mopra, the 22 m radio telescope of the Australia Telescope National Facility (ATNF), in 2003 July. The half-power beamwidth of the telescope was ~37″ at 86 GHz (Ladd et al. 2005). The front end was a dual-channel 4 K cooled SIS mixer receiver, and the typical system temperature was 200 K (SSB) at 86 GHz, including the atmosphere toward the zenith.

Two orthogonal polarizations were simultaneously observed, both tuned to the $H^{13}CO^+$ ($J = 1-0$) frequency. The spectrometer was a digital correlator with a bandwidth of 64 MHz and 2048 channels, which was divided into two 1024 channels in order to measure the two polarizations simultaneously. The velocity coverage was $\sim$110 km s^{-1} at 86 GHz, and the effective spectral resolution was $\sim$0.13 km s^{-1} at 86 GHz, corresponding to $\sim$1.2 times the channel increment.

The data were obtained with a grid spacing of 40″ in position-switching mode. The total integration time per point was $\sim$8 minutes, and the typical rms noise of the data was $\Delta T_{\rm rms} \sim$ 0.1 K at a velocity resolution of 0.1 km s^{-1}. The intensity was calibrated by using a room-temperature chopper wheel. The absolute intensity was calibrated by observing Ori KL, assuming $T_R^* = 0.55$ K (Johansson et al. 1984). The pointing accuracy was measured to be within 15″ by observing the SiO maser source RW Vel at 86 GHz every 2 hr during the observations.

2.3. *Search for Molecular Outflows*

Observations of the $J = 2-1$ transition of ^{12}CO were made with ASTE, the 10 m radio telescope of the Nobeyama Radio Observatory[6] at Pampa la Bola, Chile, in 2003 November (Kohno et al. 2004; Ezawa et al. 2004). The half-power beamwidth of the telescope was 30″ at 230 GHz. The front end was a 4 K cooled SIS mixer receiver (Sekimoto et al. 2001). The typical system temperature was 300 K (double-sideband) at 230 GHz, including the atmosphere toward the zenith. We used a digital correlator with a bandwidth of 128 MHz and 1024 channels (Sorai et al. 2000). The effective spectral resolution was 150 kHz, corresponding to a velocity resolution of 0.16 km s^{-1} at 230 GHz.

The data were obtained with a grid spacing of 30″ in position-switching mode. The total integration time per point was $\sim$1 minute, and the typical rms noise of the data was $\Delta T_{\rm rms} \sim 0.8$ K at a velocity resolution of 0.5 km s^{-1}. The intensity was calibrated by using a room-temperature chopper wheel. The absolute intensity was calibrated by observing Ori KL by assuming T_R^* to be 111 K (Sutton et al. 1985). The pointing accuracy was measured to be within 15″ as checked by optical observations of stars with a CCD camera attached to the telescope, as well as by radio observations of Jupiter and Mars.

3. RESULTS

3.1. *Distributions of* CO *Gas*

The $J = 1-0$ emission lines of carbon monoxide (^{12}CO) and its isotopes (^{13}CO and C^{18}O) have been used to study molecular clouds, since they are among the most abundant molecules in the dense interstellar medium. Although all these lines have nearly the same critical density for collisional excitation, it is found empirically that the typical densities traced by them are different: $\sim 10^2$ cm^{-3} for ^{12}CO, $\sim 10^3$ cm^{-3} for ^{13}CO, and $\sim 10^4$ cm^{-3} for C^{18}O (e.g., Mizuno et al. [1995], Onishi et al. [1996, 1998] for Taurus; Mizuno et al. [1998, 1999] for Chamaeleon; Dobashi et al. [1994, 1996], Yonekura et al. [1997], Kawamura et al. [1998], Kim et al. [2004] for a series of ^{13}CO surveys in the Milky Way; Tachihara et al. [2002] and references therein for C^{18}O cores in nearby star-forming regions). This density differentiation can be understood as follows: One of the causes for this density differentiation is due to the optical depth. The ^{12}CO transition is optically thick in most molecular clouds, making it probe the lower density enveloping layer of a molecular cloud due to photon trapping. The other two lines have smaller optical depths, allowing us to look more deeply into clouds. However, because of the selective photodissociation of the ^{13}CO and C^{18}O molecules, the abundance ratio of the isotopes varies as a function of the visual extinction A_V (e.g., Warin et al. 1996). The abundance ratio $R(^{13}\mathrm{CO}/\mathrm{C}^{18}\mathrm{O})$ reaches up to $\sim$10 near the cloud surface at $A_V \sim 1-5$. As a result, it is expected that the ^{13}CO emission mainly comes from a region of intermediate density ($\sim 10^3$ cm^{-3}) and that the C^{18}O emission comes from an inner region of high density ($\sim 10^4$ cm^{-3}).

Figure 1 shows the total-intensity distribution of ^{12}CO ($J = 1-0$) in the velocity range from $V_{\rm LSR} = -30$ to -10 km s^{-1}, overlaid on an optical image taken from the Digitized Sky Survey. We also show the distribution of OB stars overlaid on a ^{12}CO map and an Hα image in Figure 2. The positions of the OB stars are taken from the SIMBAD database. We find $\sim$80 O-type stars including 5 O3 stars, $\sim$400 B stars, and 7 Wolf-Rayet (W-R) stars in the observed area. The Hα image is reproduced from the Southern Hα Sky Survey Atlas (SHASSA; Gaustad et al. 2001). It is clearly seen that the overall distribution of the ^{12}CO emission shows an anticorrelation with the optical objects such as stellar clusters and H II regions. Most of the O-type stars are located near the η Car nebula at $(l, b) \sim (287.5, -0.7)$, creating the huge H$\alpha$ emission nebulosity, while small H II regions are formed by a few O stars such as NGC 3293 at (285.9, 0.1) and Gum 31 at (286.2, -0.2). On the other hand, there is a good correlation of the ^{12}CO emission with the optical obscuration around the η Car nebula: the northern cloud at (287.3, -0.7), the southern cloud at (287.7, -0.7), and the giant pillar at (288.0, -1.1).

In the ^{12}CO emission, a dozen intense peaks are distributed within more extended diffuse emission. The total molecular mass traced in the ^{12}CO emission is $\sim 3.5 \times 10^5\ M_\odot$, which is estimated in the following manner: We assumed an empirical relation that the molecular hydrogen column density, $N(\mathrm{H}_2)$, is proportional to the ^{12}CO integrated intensity, $I(^{12}\mathrm{CO})$. The conversion factor is called the X factor [$X = N(\mathrm{H}_2)/I(^{12}\mathrm{CO})$], and the value lies in the range $(1-3) \times 10^{20}$ cm^{-2} (K km s^{-1})$^{-1}$ toward the clouds in the Galactic disk, as estimated by the virial mass, γ-ray emission, and so on (e.g., Bloemen et al. 1986; Solomon et al. 1987; Strong et al. 1988; Bertsch et al. 1993). Here we adopted $X = 1.6 \times 10^{20}$ cm^{-2} (K km s^{-1})$^{-1}$ as derived from observations with the Energetic Gamma-Ray Experiment Telescope (EGRET; Hunter et al. 1997). The total mass of the ^{12}CO emission is estimated by using

$$M = \mu m_{\rm H} \sum D^2 \Omega N(\mathrm{H}_2 + \mathrm{He}) = 2.8 m_{\rm H} \sum D^2 \Omega N(\mathrm{H}_2), \quad (1)$$

where D is the distance, Ω is the solid angle subtended by the effective beam size ($2' \times 2'$ or $4' \times 4'$), $m_{\rm H}$ is the proton mass, and μ is the mean molecular weight. The factor of 2.8 is introduced by taking into account the contribution of helium (one He atom for every five H_2 molecules), which is the same assumption as $\mu = 2.33$. The summation is performed over the observed points within the 3 σ contour level (5 K km s^{-1}) of the integrated intensity. The distance of the η Car GMC is not well determined. Grabelsky et al. (1988) used $D = 2.7$ kpc, which is estimated from the distances of associated star clusters. Feinstein (1995) summarized the photometric data of the open clusters distributed over the entire η Car GMC and obtained the average value of 2.5 kpc. In the vicinity of η Car, values in the range 2.2–2.8 kpc

[6] Nobeyama Radio Observatory (NRO) is a branch of the National Astronomical Observatory of Japan (NAOJ), which belongs to the National Institutes of Natural Sciences (NINS).

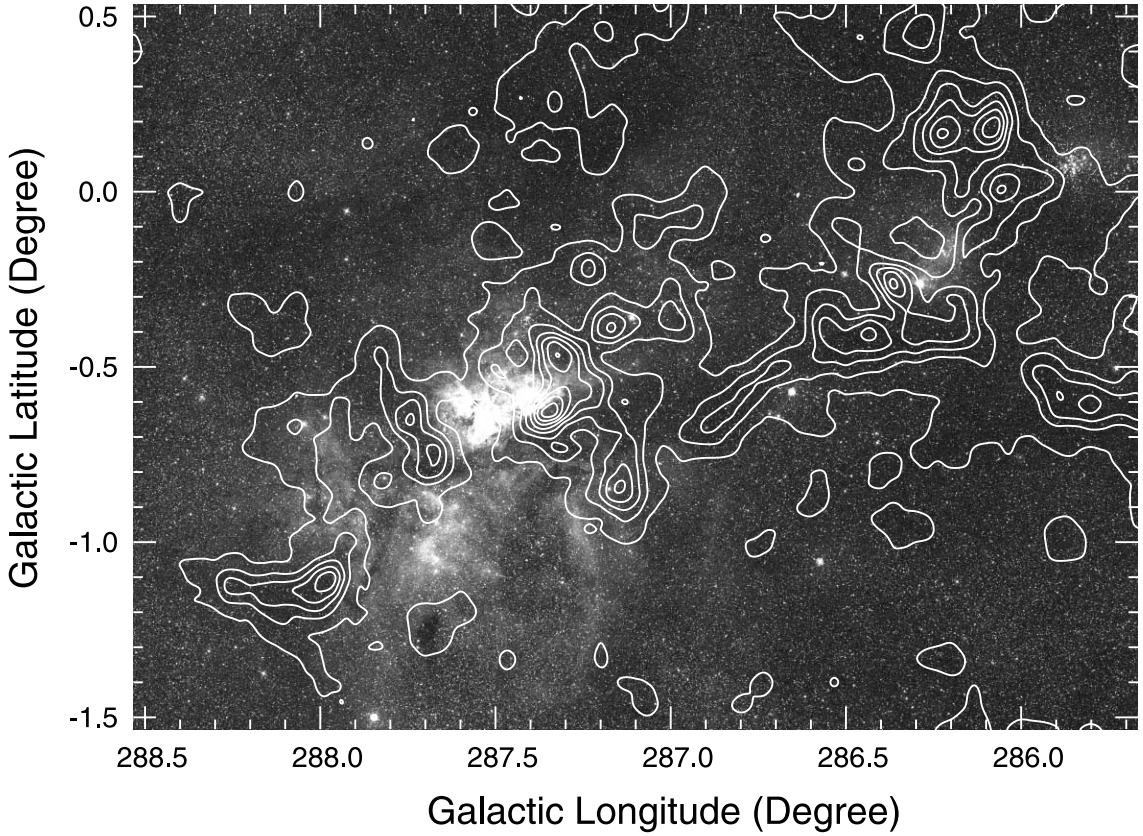

FIG. 1.—Integrated intensity map of the ^{12}CO ($J = 1-0$) emission in the velocity range $V_{LSR} = -30$ to -10 km s^{-1}, overlaid on the optical image taken from the Digitized Sky Survey. The contour levels are every 20 K km s^{-1}, starting from 5 K km s^{-1} (3 σ).

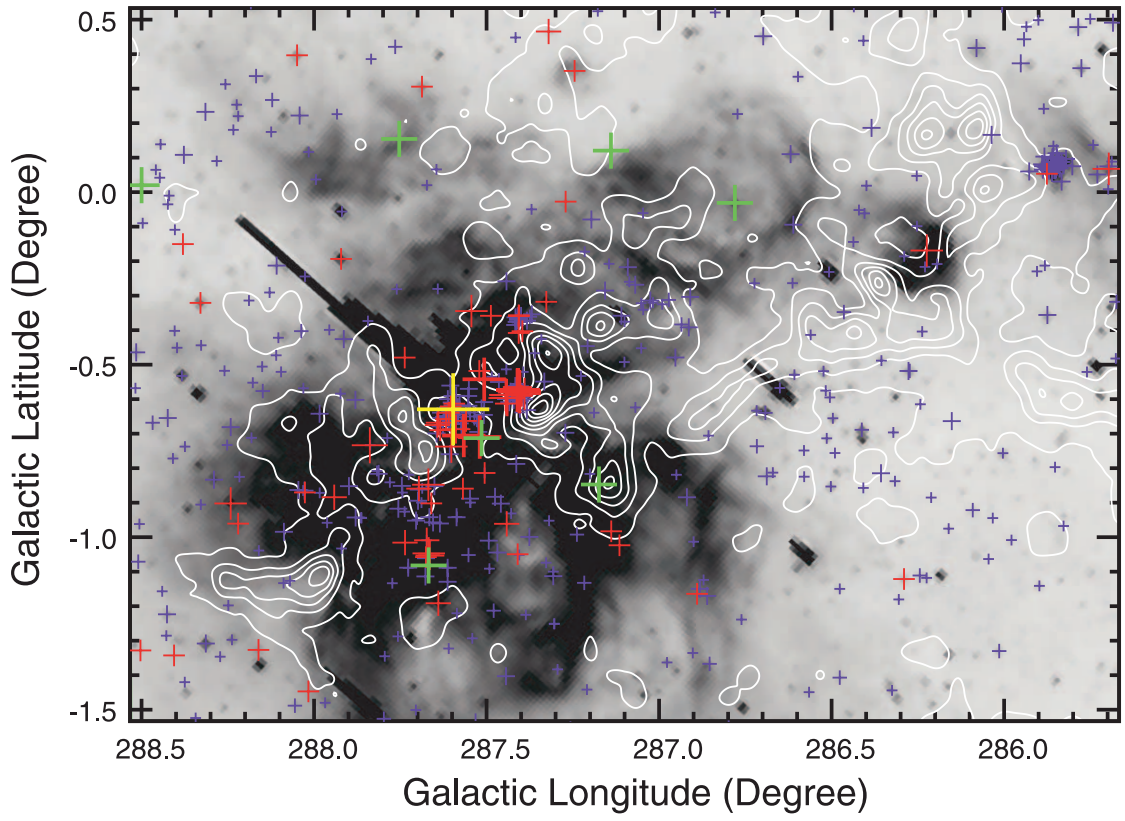

FIG. 2.—Distribution of OB stars compared with the distribution of ^{12}CO gas, overlaid on the Hα image reproduced from SHASSA. Yellow, green, red, and blue crosses denote η Car, W-R stars, O stars, and B stars, respectively. The sizes of the crosses denote the luminosity of the stars. The contour levels are the same as in Fig. 1.

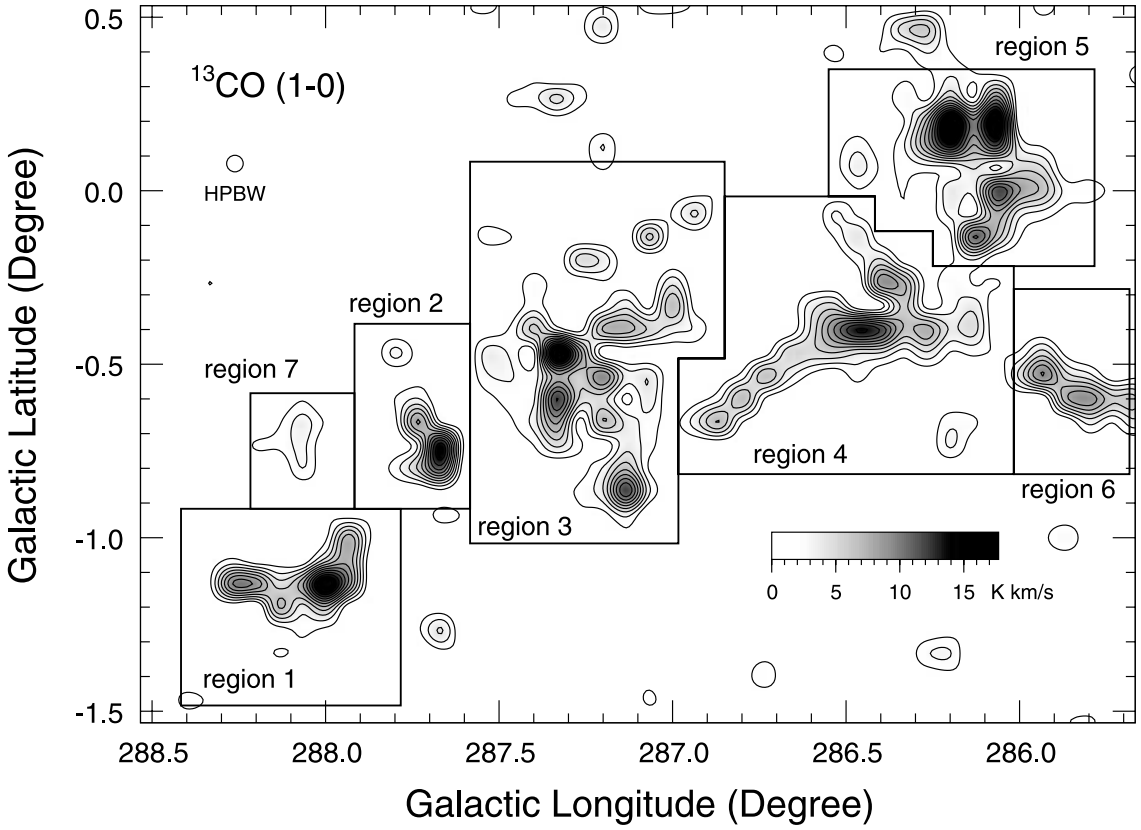

FIG. 3.—Total intensity map of ^{13}CO ($J = 1-0$) integrated over the velocity range $V_{\rm LSR} = -30$ to -10 km s^{-1}. The contour levels are every 1.35 K km s^{-1} (3 σ), starting from 1.35 K km s^{-1}.

are reported for the distances of Tr 14 and Tr 16 (e.g., Davidson & Humphreys 1997). In this paper, we adopt the frequently quoted value of 2.5 kpc as the distance of the η Car GMC (Feinstein 1995). The uncertainty in determining the total mass is estimated to be $\sim$70% from equation (1), since the distance D and the conversion factor X include $\sim$10% and $\sim$50% uncertainty, respectively. The total mass obtained in this manner is somewhat smaller than that derived by Grabelsky et al. (6.7×10^5 $M_\odot$ [1988]; cloud 11 [287.5−0.5] in their catalog), who observed the Carina arm with a 1.2 m telescope at Cerro Tololo. The difference in the total mass basically originates from the different assumptions on the X factor and the distance used in deriving the mass; they used $X = 2.8 \times 10^{20}$ cm^{-2} (K km s^{-1})$^{-1}$ and $D = 2.7$ kpc, respectively. When we use the same assumption as in Grabelsky et al. (1988), 7.2×10^5 $M_\odot$ is obtained, which is in good agreement with the value derived by Grabelsky et al. (1988).

Clumpy structure is more clearly seen in the ^{13}CO ($J = 1-0$) emission (Fig. 3). From the ^{13}CO distribution, we can divide the η Car GMC into seven regions, which are clearly separated at the 3 σ contour level (1.35 K km s^{-1}). The boundaries of the regions are similar to those in a previous study by Zhang et al. (2001b), which is based on a ^{12}CO ($J = 1-0$) map of 7.′5 grid spacing with an 8.′8 beam, but our definition traces more detailed structure. Moreover, we identified one more region (region 7). This is mainly because the spatial resolution in our study is $\sim$3 times higher than that in Zhang et al. (2001b) and because we used ^{13}CO emission instead of ^{12}CO.

The physical properties of the ^{13}CO gas are estimated in the following manner, assuming local thermodynamical equilibrium (LTE): The excitation temperature, $T_{\rm ex}$, was estimated from $T_R^*(^{12}\mathrm{CO})$ at the peak position of each C^{18}O core (see § 3.2) by using

$$T_{\rm ex} = \frac{5.53}{\ln\{1 + 5.53/[T_R^*(^{12}\mathrm{CO})(\mathrm{K}) + 0.819]\}}(\mathrm{K}). \quad (2)$$

We used the average value of the $T_{\rm ex}$ of each of the C^{18}O cores within the region as the $T_{\rm ex}$ of the region. In order to derive the ^{13}CO column density, we divide each spectrum into 0.1 km s^{-1} bins, calculate the column density within each bin, and sum them up within an LSR velocity range from -30 to -10 km s^{-1}. The optical depth in each bin, $\tau_{13}(V)$, is calculated by the following equation:

$$\tau_{13}(V) = -\ln\left(1 - \frac{T_{13}(V)}{5.29\{J_{13}[T_{\rm ex}(\mathrm{K})] - 0.164\}}\right), \quad (3)$$

where $T_{13}(V)$ is the average temperature of the ^{13}CO spectrum in each bin in units of kelvins and $J_{13}[T(\mathrm{K})] = 1/\{\exp[5.29/T(\mathrm{K})] - 1\}$. The ^{13}CO column density is estimated from

$$N_{13} = 2.42 \times 10^{14} \sum_V \frac{0.1(\mathrm{km\ s^{-1}})\tau_{13}(V)T_{\rm ex}(\mathrm{K})}{1 - \exp[-5.29/T_{\rm ex}(\mathrm{K})]}(\mathrm{cm^{-2}}). \quad (4)$$

The ratio $N(\mathrm{H_2})/N(^{13}\mathrm{CO})$ is assumed to be 5×10^5 (Dickman 1978). The mass is estimated in the same manner as for the ^{12}CO. The total molecular mass traced in the ^{13}CO emission is $\sim 1.3 \times 10^5$ $M_\odot$, which is 38% of the ^{12}CO mass.

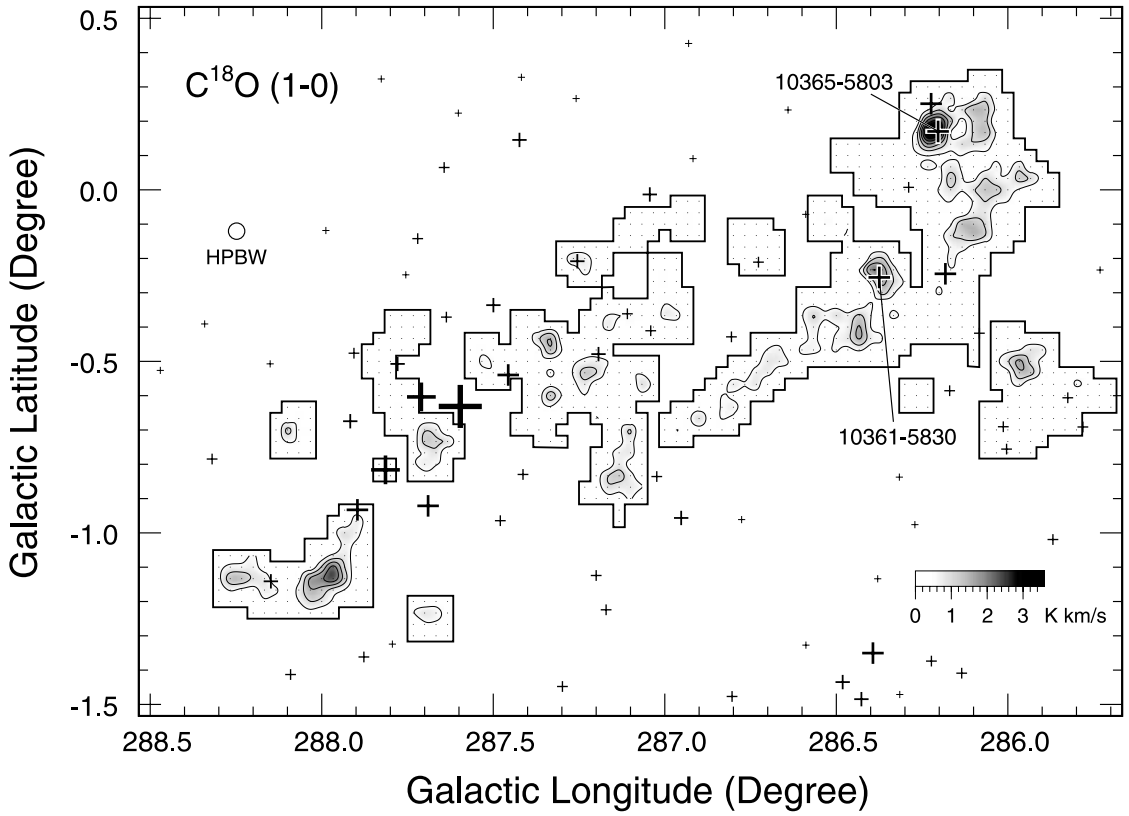

FIG. 4.—Total intensity map of $C^{18}O$ ($J = 1-0$) integrated over the velocity range $V_{LSR} = -30$ to -10 km s^{-1}. The contour levels are every 0.5 K km s^{-1} (3 σ), starting from 0.5 K km s^{-1}. *IRAS* point sources selected as candidates for protostars are also shown as crosses. The sizes of the symbols are proportional to the luminosity. Two *IRAS* point sources that are associated with $C^{18}O$ cores are labeled.

The spatial distribution of the $C^{18}O$ ($J = 1-0$) integrated intensity is shown in Figure 4. The distribution of the $C^{18}O$ gas is more compact than those of the ^{12}CO and ^{13}CO gas. The total molecular mass traced in the $C^{18}O$ emission is $\sim 5.8 \times 10^4\ M_\odot$ (see § 3.2), which is 44% of the ^{13}CO mass.

The mass of each region traced in ^{12}CO, ^{13}CO, and $C^{18}O$ is summarized in Table 1. The ratio of the ^{13}CO mass to the ^{12}CO mass ranges from 36% to 68%, with the largest value, 68%, in region 1. The ratio of the $C^{18}O$ mass to the ^{13}CO mass ranges from 21% to 72%, with the largest value, 72%, again in regions 1 and 5.

We note that CO emission with $V_{LSR} \gtrsim -10$ km s^{-1} was detected toward some areas around $(l, b) = (286.5, -0.2)$, although these velocity components are not shown in the figures. These velocity components come from distant clouds (clouds on the far side of the Carina arm at $D = 7.5$ kpc; Grabelsky et al. 1988), not associated with the η Car GMC. We will discuss these clouds in a separate paper (Y. Yonekura et al. 2005, in preparation).

3.2. *Identification of* $C^{18}O$ *Cores and their Physical Properties*

In order to investigate the physical properties of the dense regions, we define a $C^{18}O$ core in the same manner as that adopted by Onishi et al. (1996): (1) find a peak-intensity position, (2) draw a contour at the half-level of the peak intensity, (3) identify a core unless previously identified cores exist within the half-level contour, (4) find the next intensity peak outside the core, and (5) repeat the procedure after step 2 until the peak intensity falls below the 6 σ level (=1.0 K km s^{-1}).

We finally identified 15 $C^{18}O$ cores. In Figure 5 we show the boundaries of each core, and their observed properties are listed

TABLE 1
COMPARISON BETWEEN ^{12}CO, ^{13}CO, AND $C^{18}O$ MASSES IN EACH REGION

Region	l_{min} (deg)	l_{max} (deg)	b_{min} (deg)	b_{max} (deg)	M_{12}[a] ($10^4\ M_\odot$)	M_{13}[a] ($10^4\ M_\odot$)	M_{18}[a] ($10^4\ M_\odot$)	M_{13}/M_{12}	M_{18}/M_{13}	T_{ex}[b] (K)	$C^{18}O$ Cores	Associated Objects
1.....	287.800	288.400	−1.467	−0.933	2.2	1.5	1.07	0.68	0.72	20	13, 15	Giant pillar
2.....	287.600	287.900	−0.900	−0.400	1.7	0.8	0.28	0.44	0.37	20	12	η Car, southern cloud
3.....	286.867	287.567	−1.000	0.067	9.8	3.8	0.80	0.39	0.21	23	8, 9, 10, 11	η Car, northern cloud
4.....	286.033	286.967	−0.800	−0.033	8.0	3.0	1.00	0.38	0.33	21	6, 7	Gum 31
5.....	285.800	286.533	−0.200	0.333	6.6	3.2	2.29	0.48	0.72	21	2, 3, 4, 5	Gum 31, NGC 3293
6.....	285.700	286.000	−0.800	−0.300	2.0	0.7	0.27	0.36	0.38	16	1	
7.....	287.933	288.200	−0.900	−0.600	0.4	0.2	0.06	0.48	0.31	9	14	
Total					34.6	13.2	5.78	0.38	0.44			

[a] M_{12}, M_{13}, and M_{18} represent ^{12}CO mass, ^{13}CO mass, and $C^{18}O$ mass, respectively.
[b] Average value of T_{ex} of each of the $C^{18}O$ cores within the region.

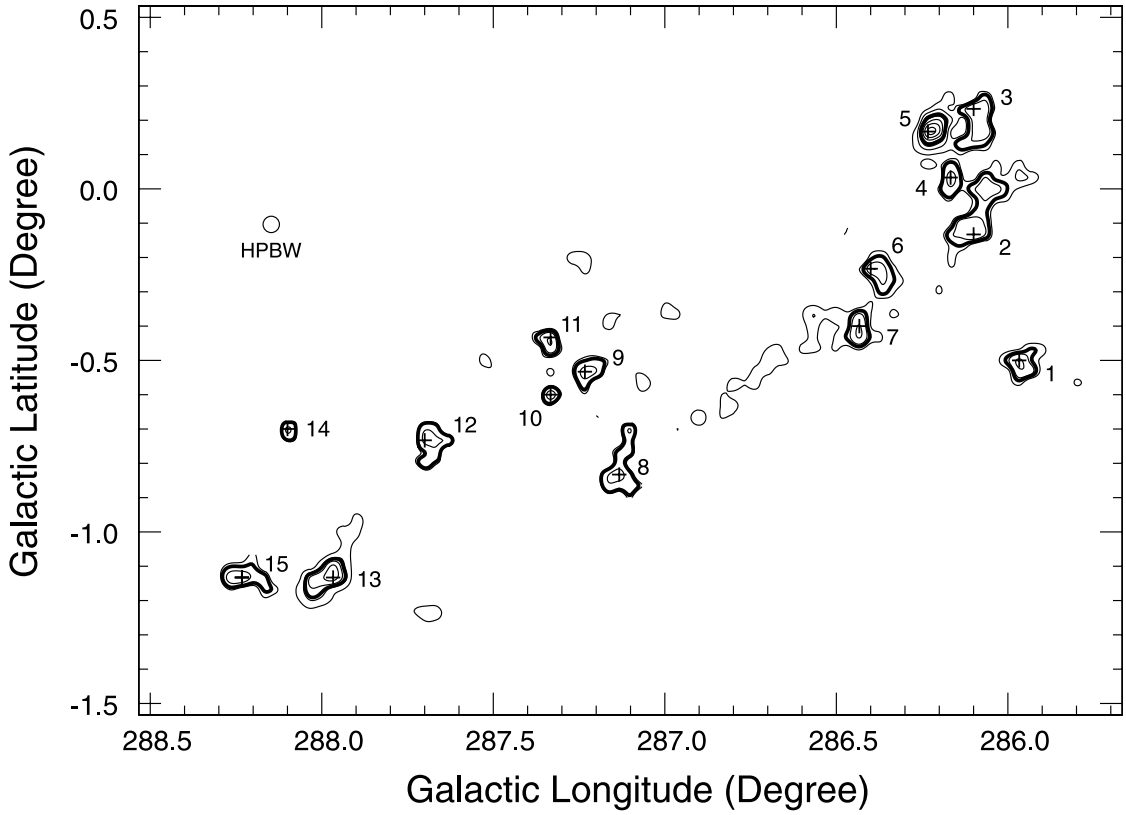

FIG. 5.—Positions of the cores indicated on a $C^{18}O$ integrated intensity map. The contour levels are the same as in Fig. 4. Thick contours represent the boundaries of each core.

in Table 2. The absolute peak temperature, $T_R^*(C^{18}O)$, the radial velocity of the $C^{18}O$ emission, V_{LSR}, and the FWHM line width, ΔV, are derived from a single Gaussian fitting for a line profile at the peak position of the core. There is a variation in the ratio of the $C^{18}O$ integrated intensity, $I(C^{18}O)$, to the ^{13}CO integrated intensity, $I(^{13}CO)$; three prominent $C^{18}O$ cores, whose $C^{18}O$ intensities at the peak position are larger than $\sim$2 K km s^{-1} (cores 5, 6, and 13), possess only moderate ^{13}CO intensity among the dozens of ^{13}CO local peaks. This indicates that ^{13}CO observation is not necessarily suited to tracing the high-density regions.

The physical properties of the $C^{18}O$ cores were estimated using nearly the same procedure as for ^{13}CO. The differences between the two procedures are as follows. The optical depth of

TABLE 2
OBSERVED PROPERTIES OF THE $C^{18}O$ CORES

NAME	COORDINATES				T_R^* ($C^{18}O$) (K)	V_{LSR} (km s^{-1})	ΔV (km s^{-1})	I_{18}[a] (K km s^{-1})	I_{13}[a] (K km s^{-1})	I_{18}/I_{13}
	l (deg)	b (deg)	α (J2000.0)	δ (J2000.0)						
1.....	285.967	−0.500	10 34 23.6	−58 46 56	0.6	−16.6	2.4	1.6	9.5	0.17
2.....	286.100	−0.133	10 36 41.1	−58 31 50	0.3	−20.7	4.5	1.4	10.6	0.14
3.....	286.100	0.233	10 38 03.5	−58 12 40	0.5	−20.6	2.6	1.4	16.5	0.09
4.....	286.167	0.033	10 37 45.3	−58 25 06	0.4	−21.6	2.6	1.2	4.3	0.28
5.....	286.233	0.167	10 38 41.8	−58 20 04	1.2	−20.0	2.9	3.6	17.6	0.20
6.....	286.400	−0.233	10 38 19.0	−58 45 54	0.5	−24.1	3.1	1.9	9.3	0.20
7.....	286.433	−0.400	10 37 54.6	−58 55 36	0.6	−13.0	2.5	1.5	13.4	0.11
8.....	287.133	−0.833	10 41 03.7	−59 38 42	0.3	−19.9	3.8	1.2	12.2	0.10
9.....	287.233	−0.533	10 42 53.0	−59 25 44	0.5	−17.6	2.6	1.2	9.4	0.13
10.....	287.333	−0.600	10 43 19.7	−59 32 05	0.3	−18.7	4.0	1.2	12.7	0.10
11.....	287.333	−0.433	10 43 56.8	−59 23 16	0.3	−19.3	5.4	1.5	17.1	0.09
12.....	287.700	−0.733	10 45 24.0	−59 49 28	0.3	−25.8	3.9	1.1	14.1	0.08
13.....	287.967	−1.133	10 45 48.2	−60 18 09	0.7	−21.3	2.8	2.3	17.2	0.13
14.....	288.100	−0.700	10 48 21.3	−59 58 44	0.5	−12.1	2.2	1.1	3.4	0.32
15.....	288.233	−1.133	10 47 43.0	−60 25 31	0.4	−17.8	3.5	1.3	9.7	0.14

NOTE.—Units of right ascension are hours, minutes, and seconds, and units of declination are degrees, arcminutes, and arcseconds.
[a] Here I_{18} and I_{13} represent the integrated intensity of the $C^{18}O$ and ^{13}CO emission, respectively.

TABLE 3
PHYSICAL PROPERTIES OF THE $C^{18}O$ CORES

Name	T_{ex} (K)	$N(H_2)$[a] (10^{21} cm^{-2})	$\langle N(H_2)\rangle$ (10^{21} cm^{-2})	r (pc)	r_{dec}[b] (pc)	M ($M_\odot$)	$n(H_2)$ (cm^{-3})	ΔV_{comp} (km s^{-1})	M_{vir} ($M_\odot$)	M_{vir}/M	*IRAS*[c]	*MSX*[d]	$H^{13}CO^+$[e]
1	16	10.6	7.4	2.0	1.8	2100	900	2.7	3000	1.4	...	...	...
2	15	9.2	6.9	3.1	2.9	4600	540	3.2	6500	1.4	...	...	...
3	21	11.1	8.4	2.7	2.5	4400	750	3.3	6100	1.4	...	...	...
4	20	9.1	7.3	1.4	1.0	1000	1200	2.6	1900	1.9	...	...	...
5	28	34.8	25.7	1.8	1.6	6100	3400	2.8	2900	0.5	1	1	1
6	26	17.3	12.8	2.0	1.8	3700	1600	3.6	5300	1.5	1	3	2
7	17	10.7	8.6	1.6	1.3	1600	1300	3.1	3200	2.0	...	...	...
8	24	10.1	7.0	2.7	2.5	3700	630	3.6	7500	2.0	...	...	...
9	21	9.7	7.3	1.6	1.3	1400	1100	2.5	2200	1.6	...	1	3
10	25	11.0	11.0	0.8	...	520	3300	4.0	2700	5.2	...	2	...
11	22	11.8	10.1	1.4	1.0	1400	1700	4.5	6100	4.3	...	...	...
12	20	8.8	6.5	2.3	2.1	2600	710	3.5	5900	2.3	...	1	...
13	20	17.4	12.8	2.2	1.9	4200	1400	4.9	11000	2.6	...	...	...
14	9	5.9	4.8	1.2	0.6	450	1000	1.9	900	2.0	...	...	...
15	19	9.9	7.0	2.0	1.8	2000	850	2.9	3500	1.8	...	...	4
Average	20	12.5	9.6	1.9	1.7	2600	1400	3.3	4600	2.1			
Median	20	10.6	7.4	2.0	1.8	2100	1100	3.2	3500	1.9			

[a] The column density for the peak position of each core.
[b] Beam-deconvolved radius of each core.
[c] Number of associated *IRAS* point sources.
[d] Number of associated *MSX* point sources.
[e] The name of the associated $H^{13}CO^+$ cores.

the $C^{18}O$ line in each bin, $\tau_{18}(V)$, is calculated by the following equation:

$$\tau_{18}(V) = -\ln\left(1 - \frac{T_{18}(V)}{5.27\{J_{18}[T_{ex}(\mathrm{K})] - 0.166\}}\right), \quad (5)$$

where $T_{18}(V)$ is the average temperature of the $C^{18}O$ spectrum in each bin in kelvins and $J_{18}[T(\mathrm{K})] = 1/\{\exp[5.27/T(\mathrm{K})] - 1\}$. The $C^{18}O$ column density is estimated from

$$N_{18} = 2.42\times10^{14}\sum_V \frac{0.1(\mathrm{km\ s^{-1}})\tau_{18}(V)T_{ex}(\mathrm{K})}{1 - \exp[-5.27/T_{ex}(\mathrm{K})]}(\mathrm{cm^{-2}}). \quad (6)$$

The ratio $N(H_2)/N(C^{18}O)$ is assumed to be 6×10^6 (Frerking et al. 1982). The mass of a $C^{18}O$ core is derived by summing over the observed points within the core. The radius of a core, r, was calculated from

$$r = \sqrt{\frac{S}{\pi}}, \quad (7)$$

where S is the area inside the core. The radius of small cores is overestimated by the beam-size effect. The relation between the observed radius, r, and the deconvolved radius, r_{dec}, is approximated by the relation

$$r_{dec} = \sqrt{r^2 - \left(\frac{\text{beam size}}{2}\right)^2}. \quad (8)$$

We also calculated the virial mass, M_{vir},

$$\frac{M_{vir}}{M_\odot} = 209\left(\frac{r}{\mathrm{pc}}\right)\left(\frac{\Delta V_{comp}}{\mathrm{km\ s^{-1}}}\right)^2, \quad (9)$$

with ΔV_{comp} defined as the FWHM line width of the composite profile derived by using a single Gaussian fitting, where the composite profile was obtained by averaging all the spectra within the core. The average H_2 number density of the core, $n(H_2)$, was derived by dividing M by the volume of the core, assuming that the core is spherical with radius r. The physical properties of the $C^{18}O$ cores thus obtained are listed in Table 3 along with the average and the median values.

Here we compare the physical properties of the cores in the η Car GMC to those of massive star–forming cores observed with the NANTEN and 4 m radio telescopes of Nagoya University: Orion B (Aoyama et al. 2001), Orion A (Nagahama 1997), Vela C (Yamaguchi et al. 1999a), Cep OB3 (Yu et al. 1996), S35/S37 (Saito et al. 1999), and Centaurus (Saito et al. 2001). All of these studies assume LTE in deriving physical properties and use the same assumption on abundance. Since the definition of a $C^{18}O$ core in Orion A, Vela C, and Cep OB3 is different from the one in this work, only values at the peak position [i.e., ΔV and $N(H_2)$] are compared for these regions. In order to be consistent for comparison, we used $(M_{vir}/M_\odot) = 209(r/\mathrm{pc})(\Delta V/\mathrm{km\ s^{-1}})^2$ instead of equation (9), and we excluded cores with serious beam-size effects, i.e., $r_{dec}/r < 0.8$, in calculating the average and median values of r, $n(H_2)$, and M_{vir}/M according to Saito et al. (2001). Hereafter, we refer to cores with $r_{dec}/r \geq 0.8$ as "resolved" cores. The average and median values in each region are listed in Table 4. The line width, ΔV, of the cores in the η Car GMC ranges from 2.2 to 5.4 km s^{-1}, with an average value of 3.2 km s^{-1}. This is the largest among the sample. The peak column density is in the range $(0.6-3.5)\times10^{22}$ cm^{-2}, with an average of 1.3×10^{22} cm^{-2}, which is a typical value for the GMCs listed here. The core mass ranges from 450 to 6100 $M_\odot$, with an average of 2600 $M_\odot$. It is difficult to compare the absolute values of the mass, since there is a dependence on the distance. The radius of the resolved cores ranges from 1.6 to 3.1 pc, with an average of 2.2 pc. The radius is also dependent on the distance. The average number density, $n(H_2)$, is in the range $(0.5-3.4)\times10^3$ cm^{-3}, with an average of

TABLE 4
AVERAGE PHYSICAL PROPERTIES OF $C^{18}O$ CORES IN MASSIVE STAR–FORMING REGIONS

Region	Distance (pc)	Number of $C^{18}O$ Cores	Number of Resolved Cores[a]	ΔV[b] (km s^{-1})	$N(H_2)$ (10^{22} cm^{-2})	M ($M_\odot$)	r[c] (pc)	$n(H_2)$[c] (10^3 cm^{-3})	M_{vir}/M[c,d]	Ref.
Orion B	400	19	18	1.7 (1.7)	2.1 (1.6)	250 (160)	0.5 (0.5)	7.6 (5.7)[e]	2.1 (1.4)[e]	1
Orion A	480	19	12	1.7 (1.6)	2.4 (1.7)	...	...	...	...	2
Vela C	700	13	10	2.5 (2.3)	2.8 (2.8)	...	...	...	...	3
Cep OB3	730	8	8	2.0 (1.9)[f]	1.5 (1.4)	...	...	...	...	4
S35/37	1800	18	4	1.7 (1.6)	1.7 (1.1)	1100 (640)	1.3 (1.3)	11.0 (9.2)	0.5 (0.6)	5
η Car GMC	2500	15	11	3.2 (2.9)	1.3 (1.1)	2600 (2100)	2.2 (2.0)	1.2 (0.9)	1.6 (1.3)	6
Centaurus III	3500	14	10	2.3 (2.3)	1.3 (1.3)	5400 (4700)	2.8 (2.8)	1.1 (1.0)[e]	0.8 (0.6)	7
Centaurus II	4500	5	5	3.1 (3.0)	1.9 (1.9)	20000 (24000)	4.2 (3.8)	1.1 (0.7)[e]	0.6 (0.5)	7
Centaurus I	5300	16	11	2.3 (2.2)	1.3 (1.0)	11000 (8600)	4.0 (3.6)	0.7 (0.7)[e]	0.5 (0.5)	7

NOTE.—Median values are given in parentheses.
[a] Number of $C^{18}O$ cores with $r_{dec}/r \geq 0.8$.
[b] FWHM line width at the peak position of the core.
[c] Values for resolved cores.
[d] Calculated by using the equation $M_{vir}/M_\odot = 209(r/\mathrm{pc})(\Delta V/\mathrm{km\ s^{-1}})^2$.
[e] Calculated in this work.
[f] Derived from the composite profile, i.e., ΔV_{comp}.
REFERENCES.—(1) Aoyama et al. 2001; (2) Nagahama 1997; (3) Yamaguchi et al. 1999b; (4) Yu et al. 1996; (5) Saito et al. 1999; (6) this work; (7) Saito et al. 2001.

1.2×10^3 cm^{-3}, which is about 1 order of magnitude smaller than the expected value for a $C^{18}O$ core, $\sim 10^4$ cm^{-3}. This is mainly due to the beam dilution; the resolution of the telescope is $\sim$2 pc at the distance of the η Car GMC, which is larger than the typical size of the $C^{18}O$ cores in Orion, $\sim$0.5 pc. The ratio of the virial mass, M_{vir}, to the LTE mass, M, ranges from 0.5 to 2.9 with an average of 1.6, which is the second largest value among the whole sample. To summarize, the cores in the η Car GMC are characterized by larger values of ΔV and M_{vir}/M on average than those in other massive star–forming regions.

3.3. *Star Formation Activity in Dense Cores: Existence of Large Numbers of Non–Star-Forming Cores*

In this subsection, we investigate the star formation activity in $C^{18}O$ cores in the η Car GMC. The *IRAS* point-source catalog is a useful database to search for young stellar objects (YSOs) embedded in molecular clouds. In order to select candidates for recently formed stars among the *IRAS* point sources, we searched for sources having cold infrared spectra defined at 25 and 60 μm, i.e., sources with higher flux densities at 60 μm than at 25 μm with a data quality better than or equal to 2 in these two bands. We excluded objects from the selection that had already been identified as planetary nebulae or external galaxies in the *IRAS* point-source catalog. Among the 316 *IRAS* point sources in the observed region, 73 were found to satisfy the criteria, and only two sources are located inside the boundaries of $C^{18}O$ cores, i.e., within the half-intensity contours: IRAS 10365−5803 and IRAS 10361−5830 are associated with $C^{18}O$ cores 5 and 6, respectively (Figs. 4 and 5). The luminosities of these sources are $\sim$30,000 $L_\odot$ (IRAS 10365−5803) and $\sim$21,000 $L_\odot$ (IRAS 10361−5830), indicating that these are candidates for massive stars or star clusters. The properties of these *IRAS* point sources are summarized in Table 5. We also searched for YSOs from the *MSX* point-source catalog. We searched for sources with a data quality better than or equal to 3 in bands C ($\sim$12 μm), D ($\sim$14 μm), and E ($\sim$21 μm). Among the 2799 *MSX* point sources in the observed region, 147 were found to satisfy the criteria, and eight sources are associated with five $C^{18}O$ cores (cores 5, 6, 9, 10, and 12; Fig. 6). The properties of these *MSX* point sources are summarized in Table 6.

The detection limit of the *IRAS* survey toward the η Car GMC is estimated to be $\sim$1000 $L_\odot$, which we derived from the distribution of the luminosity of the above 73 YSO candidate *IRAS* point sources on the assumption that these sources are located at the same distance as the η Car GMC. Therefore, we can conclude that massive star formation has not occurred in the cores without *IRAS* point sources, although we cannot exclude the existence of sources at an evolutionary stage prior to the formation of a massive star, which may not have enough emission at infrared wavelengths (e.g., Sridharan et al. 2002).

Along with the result in the next subsection, six $C^{18}O$ cores (cores 5, 6, 9, 10, 12, and 15) out of 15 (=40%) have experienced star formation, and at least 2 of 15 (=13%) are massive star–forming cores in the η Car GMC, although the proportion of star-forming cores may vary when high spatial resolution molecular line observations and more sensitive infrared and (sub-) millimeter observations are made. It should be noted that as many as

TABLE 5
PROPERTIES OF THE ASSOCIATED *IRAS* POINT SOURCES

	Coordinate				Flux Density							
Name	l (deg)	b (deg)	α (J2000.0)	δ (J2000.0)	F_{12} (Jy)	F_{25} (Jy)	F_{60} (Jy)	F_{100} (Jy)	L ($L_\odot$)	Quality	CC[a]	$C^{18}O$[b]
10365−5803	286.203	0.170	10 38 30.6	−58 19 00	7.242	85.64	1173	2782	30000	1333	CABA	5
10361−5830	286.375	−0.255	10 38 03.8	−58 46 18	12.38	38.38	625.7	2156	21000	1333	DCBD	6

NOTE.—Units of right ascension are hours, minutes, and seconds, and units of declination are degrees, arcminutes, and arcseconds.
[a] Correlation coefficient.
[b] The name of the associated $C^{18}O$ core.

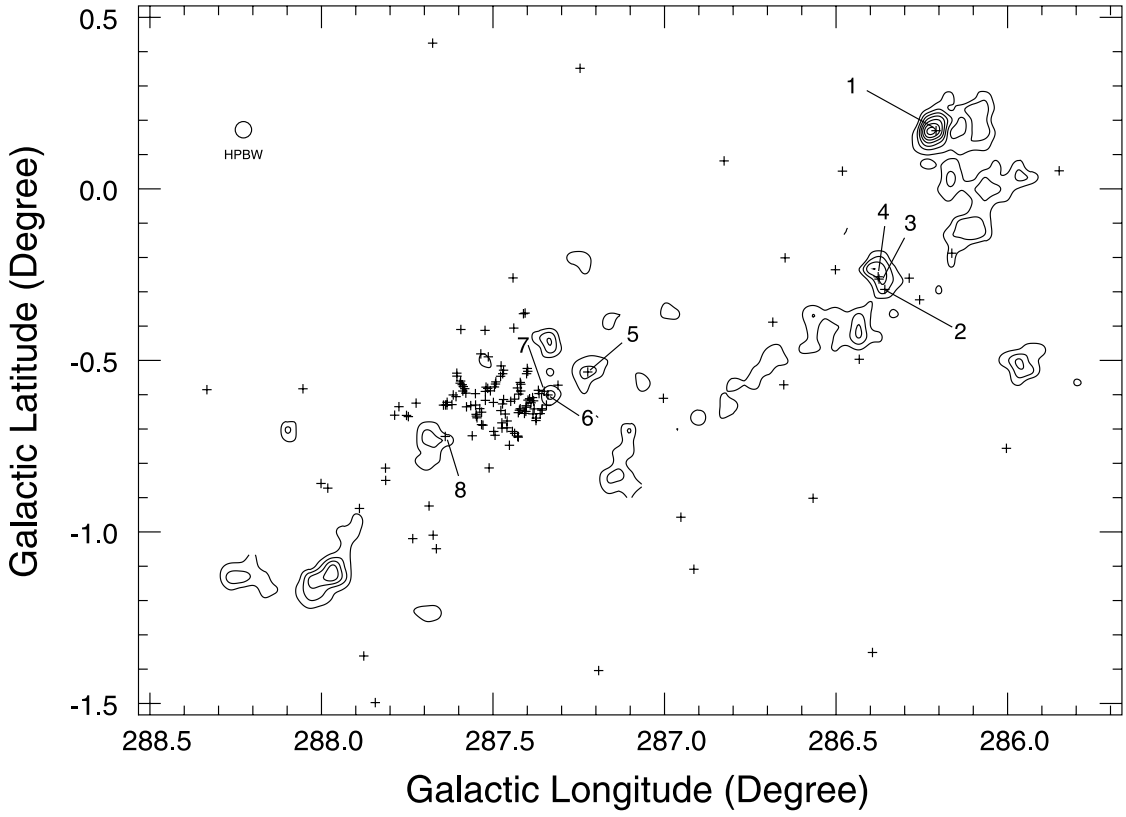

FIG. 6.—*MSX* point sources selected as candidates for protostars (*crosses*). Eight *MSX* point sources that are associated with $C^{18}O$ cores are labeled. The contour levels are the same as in Fig. 4.

13 of the 15 $C^{18}O$ cores, i.e., 87%, are not associated with luminous *IRAS* point sources ($L > 10^3\ L_\odot$). The proportion, 13%, is much lower than in other massive star–forming regions at distances within a factor of 2 of the η Car GMC: 28% in S35/S37 and 86% in Centaurus III (Saito et al. 1999, 2001). We discuss the inactiveness in detail in § 4.3.

3.4. *Search for High-Density Regions and Molecular Outflows*

In this subsection, we present the results from the search for high-density regions and molecular outflows, in order to reveal the physical properties and the evolutionary stages of dense cores, especially those without *IRAS* point sources, more precisely.

3.4.1. *Identification of* $H^{13}CO^+$ *Cores and their Physical Properties*

In order to detect high-density regions within $C^{18}O$ cores, we have observed 14 $C^{18}O$ cores (all except for $C^{18}O$ core 4) in $H^{13}CO^+$ ($J = 1-0$) emission, which traces a typical density of $\sim 10^5$ cm^{-3} (e.g., Mizuno et al. 1994; Onishi et al. 2002). Therefore, the $C^{18}O$ cores without *IRAS* point sources, which are detected in $H^{13}CO^+$ emission, can be considered good candidates for sites of future massive star formation. Significant $H^{13}CO^+$ emission above the 3 σ noise level was detected toward four $C^{18}O$ cores (cores 5, 6, 9, and 15), two of which (cores 5 and 6) have associated *IRAS* point sources and three of which (cores 5, 6, and 9) have *MSX* point sources (see § 3.3). Distributions of $H^{13}CO^+$

TABLE 6
PROPERTIES OF THE ASSOCIATED *MSX* POINT SOURCES

		Coordinate				Flux Density					
No.	Name	l (deg)	b (deg)	α (J2000.0)	δ (J2000.0)	Band A (Jy)	Band C (Jy)	Band D (Jy)	Band E (Jy)	Quality	$C^{18}O$[a]
1.....	MSX6C G286.2086+00.1694	286.2086	0.1694	10 38 32.5	−58 19 12	1.3532	2.8816	7.1817	40.572	4444	5
2.....	MSX6C G286.3579−00.2933	286.3579	−0.2933	10 37 48.4	−58 47 48	0.71259	1.8153	2.6774	6.0653	4344	6
3.....	MSX6C G286.3747−00.2630	286.3747	−0.2630	10 38 02.0	−58 46 43	3.5907	4.7559	2.4093	7.5775	4444	6
4.....	MSX6C G286.3773−00.2563	286.3773	−0.2563	10 38 04.6	−58 46 26	1.6278	2.9183	3.8554	12.095	4444	6
5.....	MSX6C G287.2238−00.5339	287.2238	−0.5339	10 42 48.9	−59 25 29	1.2040	1.6909	1.5151	4.3560	4344	9
6.....	MSX6C G287.3399−00.6008	287.3399	−0.6008	10 43 22.3	−59 32 19	0.80028	2.9386	5.9723	12.516	4444	10
7.....	MSX6C G287.3506−00.5900	287.3506	−0.5900	10 43 29.2	−59 32 03	0.55922	2.0313	3.9602	7.9096	4444	10
8.....	MSX6C G287.6393−00.7219	287.6393	−0.7219	10 45 00.9	−59 47 10	3.4863	4.2647	3.6021	17.835	4444	12

NOTE.—Units of right ascension are hours, minutes, and seconds, and units of declination are degrees, arcminutes, and arcseconds.
[a] The name of the associated $C^{18}O$ core.

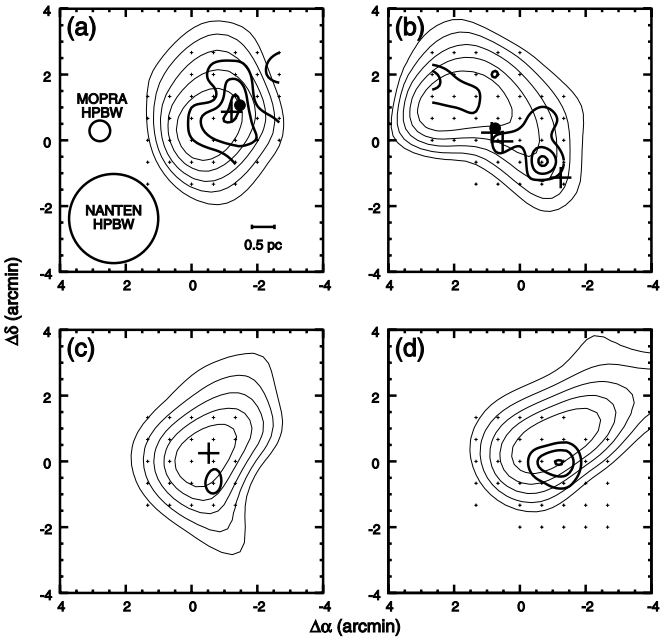

FIG. 7.—(*a*) Distribution of the $H^{13}CO^+$ ($J = 1-0$) emission toward $C^{18}O$ core 5. The thick contours represent $H^{13}CO^+$ intensity integrated over the velocity range -23 km s^{-1} $\leq V_{LSR} \leq -16$ km s^{-1}. Contour levels are every 0.4 K km s^{-1} (3 σ), starting from 0.4 K km s^{-1}. The thin contours represent the distribution of the $C^{18}O$ core observed by NANTEN, with contour levels of 50%, 60%, 70%, 80%, and 90% of the peak intensity. The coordinates are shown in offsets from the reference position ($\alpha_{2000} = 10^h38^m41^s.8$, $\delta_{2000} = -58°20'4''$). The filled circle and the cross denote *IRAS* and *MSX* point sources, respectively. (*b*) Same as (*a*), but for $C^{18}O$ core 6. The velocity range, the 3 σ level, and the reference position are -30 km s^{-1} $\leq V_{LSR} \leq -20$ km s^{-1}, 0.42 K km s^{-1}, and ($10^h37^m58^s.0$, $-58°46'40''$), respectively. (*c*) Same as (*a*), but for $C^{18}O$ core 9. The velocity range, the 3 σ level, and the reference position are -20 km s^{-1} $\leq V_{LSR} \leq -16$ km s^{-1}, 0.35 K km s^{-1}, and ($10^h42^m53^s.0$, $-59°25'44''$), respectively. (*d*) Same as (*a*), but for $C^{18}O$ core 15. The velocity range, the 3 σ level, and the reference position are -20 km s^{-1} $\leq V_{LSR} \leq -16$ km s^{-1}, 0.45 K km s^{-1}, and ($10^h47^m57^s.5$, $-60°26'26''$), respectively.

emission are presented in Figure 7. In order to study the physical properties, we define the $H^{13}CO^+$ cores in the same manner as we do $C^{18}O$ cores. As a result, we identified three cores.

The physical properties of the $H^{13}CO^+$ cores were estimated using the same method as for $C^{18}O$: The $H^{13}CO^+$ optical depth in each bin, τ_V, is calculated from

$$\tau(H^{13}CO^+)_V = -\ln\left\{1 - \frac{T(H^{13}CO^+)_V}{4.16[J(T_{ex}) - 0.272]}\right\}, \quad (10)$$

where $J(T) = 1/[\exp(4.16/T) - 1]$. We tentatively estimate T_{ex} of each $H^{13}CO^+$ core from the ^{12}CO ($J = 2-1$) observations (see § 3.4.2), since the beam sizes of both observations are similar. The $H^{13}CO^+$ column density, $N(H^{13}CO^+)$, is estimated by using the following equation:

$$N(H^{13}CO^+) = 1.92 \times 10^{11} \times \sum_V \frac{0.1(\text{km s}^{-1})\tau(H^{13}CO^+)_V T_{ex}(K)}{1 - \exp[-4.16/T_{ex}(K)]} (\text{cm}^{-2}). \quad (11)$$

The H_2 column density, $N(H_2)$, was derived from $N(H^{13}CO^+)$ by making the same assumption as in Aoyama et al. (2001): $[HCO^+]/[H_2] = 4.0 \times 10^{-9}$ and $^{12}C/^{13}C = 89$. The assumption of T_{ex} may not be correct, since the density is perhaps smaller than the critical density of $H^{13}CO^+$ ($J = 1-0$), i.e., the $J = 1-0$ line of $H^{13}CO^+$ is perhaps subthermally excited. However, the uncertainty in T_{ex} would not seriously affect the estimate of the column density N: even if we changed the value of T_{ex} by a factor of 2, the estimated value of N changes within a factor of 1.9, which is smaller than the uncertainty in the HCO^+ abundance (e.g., Bergin et al. 1997; Jørgensen et al. 2004).

The physical properties of the $H^{13}CO^+$ cores are listed in Table 7. The total mass of the molecular gas traced by $H^{13}CO^+$ in the observed area above the 3 σ level is estimated to be $\sim$4300 $M_\odot$, corresponding to $\sim$7% of the $C^{18}O$ mass.

It is to be noted that a significant difference is found in the behavior of the line width between cores with and without *IRAS* point sources: the line widths in the $H^{13}CO^+$ cores are much smaller than those in the $C^{18}O$ cores for the cores without *IRAS* point sources (cores 9 and 15), whereas the line widths in the $H^{13}CO^+$ cores are nearly the same as or somewhat larger than those in $C^{18}O$ cores for cores with *IRAS* point sources (cores 5 and 6). The present result can be compared to the multitracer, single-cloud line width–size relation, which is classified as type 3 in Goodman et al. (1998). The relation $\Delta V \propto R^a$ with $0.2 \lesssim a \lesssim 0.7$ is reported with the tendency that massive star–forming regions tend to have lower values of a (e.g., Caselli & Myers 1995). The present result is consistent with the above tendency in the sense that the value of a in massive star–forming cores tends to be smaller than in the others, although the trend is more extreme; i.e., $a \lesssim 0$. The trend might be indicating that line width enhancement due to the input of turbulence by the activity of star formation, such as jets and molecular outflows, is effective especially near the center of the massive star–forming cores. However, we have to wait until statistically more accurate studies can be made based on a large sample.

This section can be summarized as follows. We detected $H^{13}CO^+$ emission from four $C^{18}O$ cores, which indicates that high-density gas is presented in these cores and that these cores are

TABLE 7
PHYSICAL PROPERTIES OF $H^{13}CO^+$ CORES

Name	α (J2000.0)	δ (J2000.0)	T_R^* (K)	V_{LSR} (km s^{-1})	ΔV (km s^{-1})	T_{ex} (K)	τ	$N(H_2)$ (10^{22} cm^{-2})	r (pc)	ΔV_{comp} (km s^{-1})	M ($M_\odot$)	M_{vir} ($M_\odot$)	$\langle N(H_2)\rangle$ (10^{22} cm^{-2})	$n(H_2)$ (10^4 cm^{-3})	$C^{18}O$[a]
1.....	10 38 31.7	−58 18 44	0.38	−19.4	2.9	30	0.018	4.5	0.77	3.8	1400	2300	3.4	1.1	5
2.....	10 37 52.9	−58 47 20	0.41	−22.5	3.0	55	0.011	7.6	0.27	3.0	400	500	7.6	6.8	6
3.....	10 42 47.8	−59 26 24	0.35	−17.3	1.3	35	0.017	2.0	...	...	...	...	...	...	9
4.....	10 47 46.7	−60 26 26	0.81	−17.8	1.6	30	0.035	5.0	0.39	1.6	470	200	4.4	2.8	15

NOTE.—Units of right ascension are hours, minutes, and seconds, and units of declination are degrees, arcminutes, and arcseconds.
[a] The name of the associated $C^{18}O$ core.

capable of star formation. Indeed, two (cores 5 and 6) have already experienced massive star formation, and another one (core 9) has experienced less massive star formation. The other $C^{18}O$ core (No. 15) may not yet have experienced star formation, which makes the core the most probable site for future star formation, although we cannot rule out the possibility that less massive stars are forming inside (see § 3.4.2).

3.4.2. *Molecular Outflows*

It is well known that molecular outflows are ubiquitous in low-mass star formation (Lada 1985; Fukui et al. 1986, 1993; Fukui 1989 and references therein), and they are believed to be related to the accretion process. It is also suggested by these studies that molecular outflows are also common in massive star–forming regions. Recent systematic surveys for outflows toward regions of massive star formation showed a detection rate of molecular outflow phenomena as high as ∼90%, confirming that outflows are also common in massive star–forming regions (e.g., Shepherd & Churchwell 1996; Zhang et al. 2001a; Beuther et al. 2002b). The formation process of massive stars is, however, still controversial; it is not yet known whether massive stars are formed by direct accretion on a central protostar through an accretion disk (e.g., McKee & Tan 2003) or by the coalescence of low- to intermediate-mass protostars (Bonnell et al. 1998). At any rate, the detection of a molecular outflow is a direct indication of ongoing star formation. The age and the luminosity of the driving source can be estimated from the observations, and moreover, the kinematic information, such as the interaction with parent molecular clouds, as well as the systemic velocity of the driving source, can be used to solve the distance ambiguity in cases for which more than one molecular cloud is located in the same line of sight.

We searched for molecular outflows toward seven $C^{18}O$ cores (Nos. 5–9, 14, and 15). We detected one outflow, as well as three candidates for outflows. Figure 8 displays the ^{12}CO spectra around $C^{18}O$ core 15. In the figure, both the blueshifted (-35 km s^{-1} ≤ V_{LSR} ≤ -25 km s^{-1}) and redshifted (-15 km s^{-1} ≤ V_{LSR} ≤ -5 km s^{-1}) wings are clearly seen in some spectra, where the velocity ranges for wing components are determined at a 1 σ noise level in the spectra smoothed to the velocity resolution of 0.5 km s^{-1} ($T_R^* \sim 0.8$ K): the blueshifted component is prominent at the offset $(\Delta\alpha, \Delta\delta) = (-1', 0')$, while the red is most intense at $(-0.'5, 0')$. The distribution of the ^{12}CO line intensities integrated between $V_{LSR} = -35$ and -25 km s^{-1} (blue component) and between -15 and -5 km s^{-1} (red component) is shown in Figure 9.

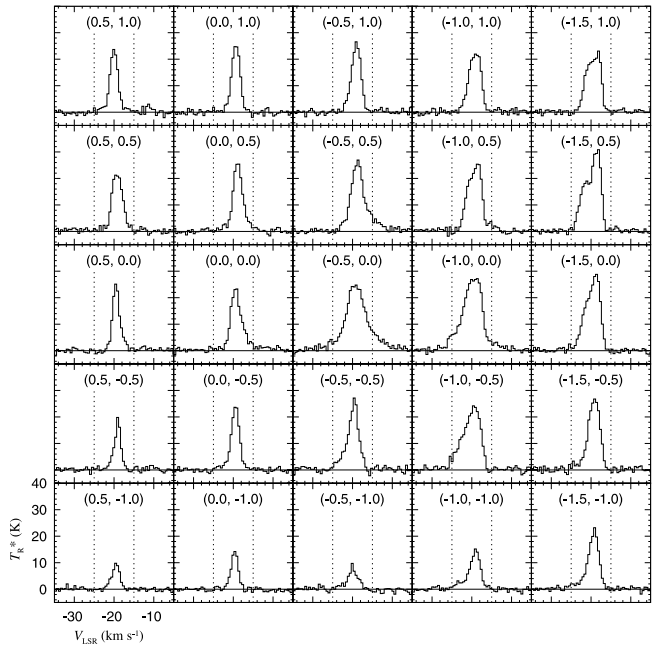

FIG. 8.—^{12}CO spectra observed toward $C^{18}O$ core 15. The offsets from the position $(\alpha_{2000}, \delta_{2000}) = (10^h47^m57^s.5, -60°26'26'')$ are shown in parentheses in units of arcminutes. The spectra are smoothed to a velocity resolution of 0.5 km s^{-1}.

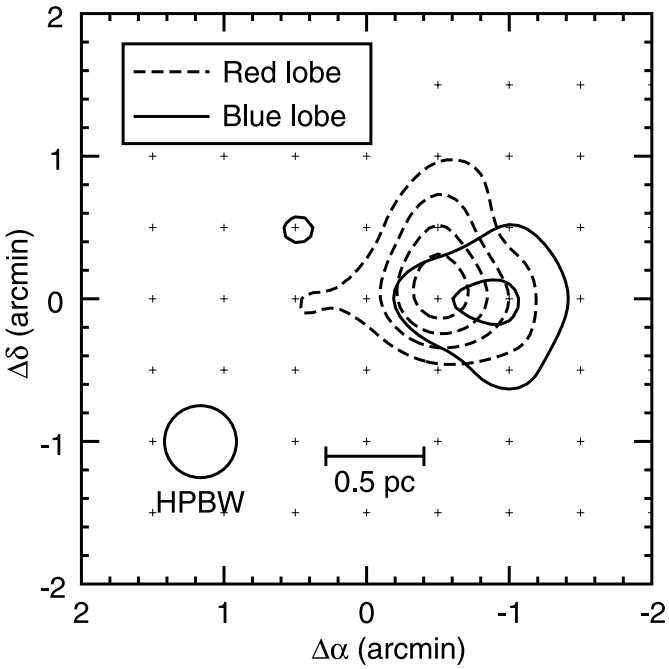

FIG. 9.—Distribution of the molecular outflow within $C^{18}O$ core 15. The solid contours represent the ^{12}CO intensity of the blue component integrated between $V_{LSR} = -35$ and -25 km s^{-1}, and the dashed contours show that of the red component between $V_{LSR} = -15$ and -5 km s^{-1}. Contours are every 5 K km s^{-1} (3 σ), starting from 5 K km s^{-1}.

Figure 10 shows ^{12}CO profiles of three outflow candidates. Although their spectra show asymmetry or have broad wing features, we cannot make a contour map of the wing components, due to the existence of multiple velocity components and/or contamination from the emission at the OFF position.

Physical parameters of the detected outflow associated with $C^{18}O$ core 15 were estimated as follows. The excitation temperature of the high-velocity gas was assumed to be the same as

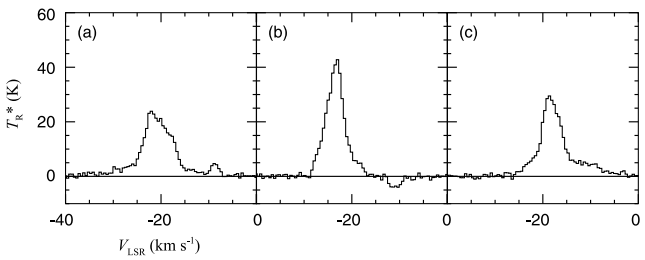

FIG. 10.—^{12}CO profiles for the outflow candidates. The positions are (*a*) $\alpha_{2000} = 10^h38^m34^s.2$, $\delta_{2000} = -58°19'34''$ [$(\Delta\alpha, \Delta\delta) = (-1', 0'.5)$ offset from the reference position in Fig. 7*a*], (*b*) $\alpha_{2000} = 10^h37^m54^s.1$, $\delta_{2000} = -58°46'40''$ [$(\Delta\alpha, \Delta\delta) = (-0'.5, 0')$ offset from the reference position in Fig. 7*b*], and (*c*) $\alpha_{2000} = 10^h42^m49^s.0$, $\delta_{2000} = -59°25'44''$ [$(\Delta\alpha, \Delta\delta) = (-0'.5, 0')$ offset from the reference position in Fig. 7*c*].

TABLE 8
PROPERTIES OF THE OUTFLOW

Component	V_{range}[a] (km s^{-1})	V_{char}[b] (km s^{-1})	Size[c] (pc)	Radius (pc)	Mass ($M_\odot$)	Kinetic Energy (10^{45} ergs)	Mechanical Luminosity ($L_\odot$)	Momentum ($M_\odot$ km s^{-1})	Dynamical Timescale (10^4 yr)
Blue	(−35, −25)	16.5	0.41	0.41	1.2	1.7	0.39	14	2.4
Red	(−15, −5)	13.5	0.41	0.55	2.1	1.9	0.37	20	4.0

[a] Velocity range where the high-velocity emission is detected at >1 σ noise level ($T_R^* \sim 0.8$ K).
[b] Maximum velocity shift of the ^{12}CO ($J = 2-1$) emission from $V_{LSR} = -18.5$ km s^{-1}.
[c] The maximum separation of the outflow lobes from the position of the driving source.

that of the quiescent gas, and estimated to be 30 K from the ^{12}CO ($J = 2-1$) observations by using the equation

$$T_{ex} = \frac{11.1}{\ln\{1 + 11.1/[T_R^*(^{12}\mathrm{CO},\ 2-1)(\mathrm{K}) + 0.187]\}}(\mathrm{K}). \quad (12)$$

The column densities of ^{12}CO ($J = 2-1$) are calculated under the assumption of LTE using the following equation:

$$N(\mathrm{CO}) = 1.04 \times 10^{13} T_{ex} \exp\left(\frac{16.6}{T_{ex}}\right) \frac{1}{\beta} \int T_R^*(^{12}\mathrm{CO})\, dV, \quad (13)$$

where the integration is made over the wing component; β is defined from the ^{12}CO optical depth as $\beta = [1 - \exp(-\tau)]/\tau$. We assumed $\tau = 2$ for both the red and blue components, which is a typical value for outflows observed in the ^{12}CO ($J = 2-1$) line (Levreault 1988). The column density of H_2 molecules was estimated using an $[H_2]/[CO]$ ratio of 1×10^4 (Frerking et al. 1982). The mass of each component is derived using equation (1) with an effective beam size of $30'' \times 30''$. The summation is performed over the observed points within the 3 σ contour level (5 K km s^{-1}) of the intensity integrated over the wing component. Sizes of the lobes are defined at the 3 σ contour level of the integrated intensity map of the outflow. We tentatively defined the position of the driving source of this outflow as the center of the peak position of each lobe because no driving sources, such as *IRAS* and *MSX* point sources, have been identified around the outflow yet. The radius is defined as the maximum separation between the position of the driving source and the 3 σ contour of the wing emission.

Using the mass and the radius of the outflow, we estimate the kinetic energy, mechanical luminosity, momentum, and dynamical timescale of the outflow in the same manner as in Yonekura et al. (1998). We calculated physical properties of the outflow for the velocity ranges from −35 to −25 km s^{-1} for the blueshifted wing and from −15 to −5 km s^{-1} for the redshifted wing.

These values are summarized in Table 8. The nature of the driving source is not clear because no sources have been identified yet around the outflow. We estimate the upper limit to the luminosity from the *IRAS* sky survey atlas to be 3900 $L_\odot$. Another estimate for the luminosity can be made by using the empirical relation between the mechanical luminosity of the outflow and the bolometric luminosity of the driving source (Cabrit & Bertout 1992); 15 $L_\odot$ is obtained in this manner. There are two possibilities for the nature of the driving source: (1) a less massive star with a luminosity below the *IRAS* and/or *MSX* detection limit or (2) a source at an evolutionary stage prior to the formation of a star without enough emission in the infrared (e.g., Sridharan et al. 2002). We cannot rule out either of the above two possibilities at the moment, but the former might be more probable because the dynamical timescale ($\sim 3 \times 10^4$ yr), which is probably overestimated because of the overestimation of size due to low angular resolution, is relatively long. High-resolution CO observations, as well as submillimeter dust continuum observations, will reveal the nature of the driving source.

4. DISCUSSION

4.1. *Physical Properties of* $C^{18}O$ *Cores and Their Relation to Star Formation*

Here we discuss the relationship between the star formation activity and the physical properties of $C^{18}O$ cores, which has become possible thanks to the detection of a large number of cores without any signs of star formation. In the study of $C^{18}O$ cores in Orion B, Aoyama et al. (2001) found that star formation occurs preferentially in cores with larger ΔV, N, and M and that the luminosity of the forming stars increases with N. In Centaurus, the luminosity of the forming stars increases with N and M, as well as ΔV, and decreases with M_{vir}/M (Saito et al. 2001). Saito et al. (2001) also found that the luminosity increases with ΔV by compiling the data in Orion A and B, S35, Vela C, and Centaurus and proposed the possibility that the mass of forming stars is determined by ΔV, since high mass accretion rates can be achieved in cores with large ΔV. However, it is controversial whether large ΔV is a cause or effect of massive star formation.

We divided the $C^{18}O$ cores into three groups: (A) cores with *IRAS* point sources (Nos. 5 and 6), (B) other star-forming cores (Nos. 9, 10, 12, and 15), and (C) cores without any signs of star formation. The cores in group A are thought to be sites of massive star formation (see Table 5 for the luminosities of the associated *IRAS* point sources). There are two possibilities for the nature of the cores in group B; these are either (1) less massive stars with luminosities below the *IRAS* detection limit or (2) sources at an evolutionary stage prior to the formation of stars without enough emission in the infrared (see § 3.4.2). Here we tentatively treat them as less massive star–forming cores, following the argument in § 3.4.2. The cores in group C seem to be sites of less active star formation than those in groups A and B, which is inferred from the absence of the high-density regions (see § 3.4.1). Table 9 gives the average physical properties of these three groups, as well as the average of all cores in the η Car GMC. We also calculated the average properties of all the star-forming cores, i.e., cores in groups A and B. Figure 11 shows a series of histograms of the core parameters, (*a*) line width ΔV_{comp}, (*b*) H_2 column density $N(H_2)$, (*c*) LTE mass M, (*d*) radius r, (*e*) H_2 number density $n(H_2)$, and (*f*) ratio M_{vir}/M. Note that only resolved cores are used to make the histograms of r, $n(H_2)$, and M_{vir}/M.

It is clearly seen that $N(H_2)$, M, and $n(H_2)$ are larger and the ratio M_{vir}/M is smaller in group A than in groups B and C, while

TABLE 9
AVERAGE PHYSICAL PROPERTIES OF $C^{18}O$ CORES IN THE η Car GMC

Type of Core	Group[a]	Name[b]	ΔV_{comp} (km s^{-1})	$N(H_2)$ (10^{21} cm^{-2})	M ($M_\odot$)	r[c] (pc)	$n(H_2)$[c] ($\times 10^3$ cm^{-3})	M_{vir}/M[c]
Cores with *IRAS* point sources.....	A	5, 6	3.2 (3.2)	26.1 (26.1)	4900 (4900)	1.9 (1.9)	2.5 (2.5)	1.0 (1.0)
Other star-forming cores.....	B	9, (10), 12, 15	3.2 (3.2)	9.9 (9.8)	1600 (1700)	2.0 (2.0)	0.9 (0.9)	1.9 (1.8)
All star-forming cores.....	A+B	5, 6, 9, (10), 12, 15	3.2 (3.2)	15.3 (10.5)	2700 (2300)	2.0 (2.0)	1.5 (1.1)	1.5 (1.6)
Non–star-forming cores.....	C	1, 2, 3, (4), 7, 8, (11), 13, (14)	3.3 (3.2)	10.7 (10.6)	2600 (2100)	2.4 (2.4)	0.9 (0.8)	1.8 (1.7)
All $C^{18}O$ cores.....	...	All	3.3 (3.2)	12.5 (10.6)	2600 (2100)	2.2 (2.0)	1.2 (0.9)	1.7 (1.6)

NOTE.—Median values are given in parentheses.
[a] See § 4.1.
[b] The names of the associated $C^{18}O$ cores. The names of the unresolved cores are given in parentheses.
[c] Values for resolved cores.

the tendency is not clear in ΔV_{comp} and r (trend 1). Between star-forming cores (groups A+B) and non–star-forming cores (group C), $N(H_2)$ and $n(H_2)$ are larger in groups A+B than in group C (trend 2). However, no significant difference between group B and group C is seen (trend 3). These trends (trends 1–3) might be indicating the differences in the physical properties among the cores as a function of the masses of the forming stars.

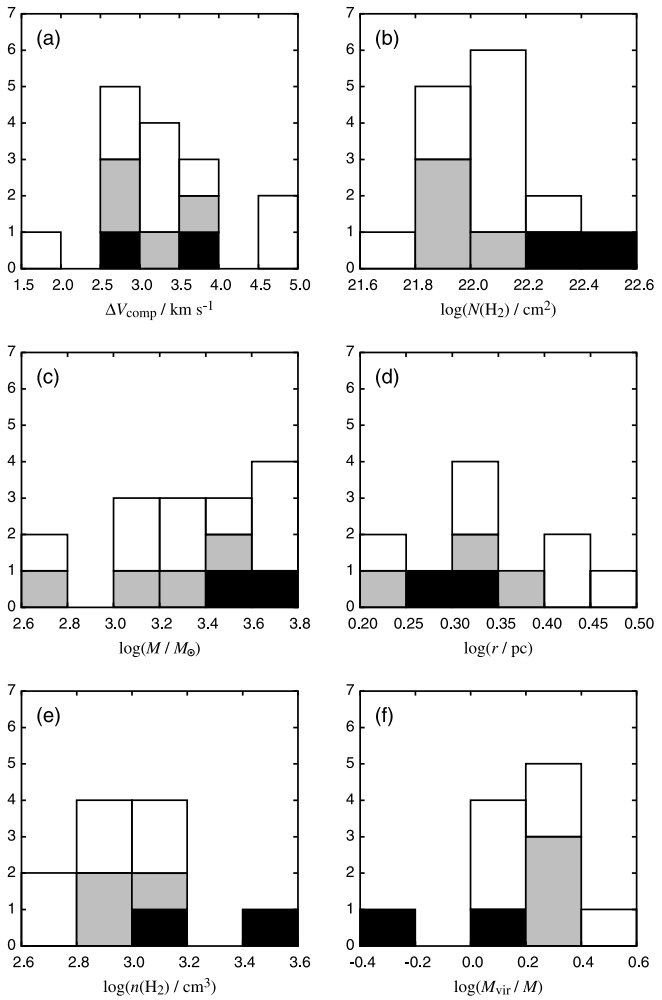

FIG. 11.—Histograms of (*a*) line width, (*b*) H_2 column density, (*c*) mass, (*d*) radius, (*e*) average H_2 number density, and (*f*) ratio M_{vir}/M of cores in the three groups. The dark-shaded and light-shaded regions indicate massive star–forming cores (group A) and less massive star–forming cores (group B), respectively. The open regions indicate less active star-forming cores (group C). Note that only resolved cores are used to make the histograms of r, $n(H_2)$, and M_{vir}/M.

Here we compare the present results to those in Centaurus (Saito et al. 2001). In Centaurus, the luminosity of the forming stars increases with N and M, as well as ΔV, and decreases with M_{vir}/M. This trend is the same as trend 1 in the η Car GMC except for ΔV. Although we have obtained 127 $C^{18}O$ cores in massive star–forming regions so far by using the same telescope, including 15 in the η Car GMC, we cannot make a direct comparison at present, because of the differences in the detection limit and/or the definition of $C^{18}O$ cores. The results of a detailed comparison will be published in a separate paper.

We can conclude that massive star formation occurs preferentially in cores with larger N, M, and n and smaller M_{vir}/M in η Car GMC. High spatial resolution and high-sensitivity observations in the infrared (e.g., *Spitzer Space Telescope*, *Astro-F*), as well as observations in high-density tracers such as CS ($J = 7-6$), HCO^+ ($J = 4-3$), and HCN ($J = 4-3$) (e.g., ASTE), will help to reveal the properties of $C^{18}O$ cores.

4.2. *Comparison with Submillimeter Observations*

It is of interest to compare the distribution of CO and $C^{18}O$ ($J = 1-0$) emissions to that of CO ($J = 4-3$) emission obtained with the Antarctic Submillimeter Telescope and Remote Observatory (AST/RO; Zhang et al. 2001b), since different excitation conditions are required between CO ($J = 4-3$) and CO ($J = 1-0$). The $J = 4$ level of the CO molecule is 55 K above the ground level, and the critical density of the $J = 4-3$ transition is $\sim 8 \times 10^4$ cm^{-3} for the optically thin case, whereas the $J = 1$ level of the CO molecule is 5.5 K above the ground level, and the critical density of the $J = 1-0$ transition is $\sim 10^3$ cm^{-3}. At a kinetic temperature of 40 K, the $J = 4-3$ emission of CO is most intense at a density of $\sim 10^5$ cm^{-3}, while the $J = 1-0$ intensity peaks at around 10^3 cm^{-3} (Goldsmith & Langer 1978). Observationally, the density effectively emitting these emissions may correspond to somewhat lower than these values ($\sim 10^2$ cm^{-3} for the $J = 1-0$ emission), which can be understood if we take into account the optical depth effect. Thus, the CO ($J = 4-3$) line requires higher temperature and density than the CO ($J = 1-0$) line. However, the overall distribution of the molecular gas traced in the CO ($J = 1-0$) line and that of the CO ($J = 4-3$) line is quite similar except the following two regions:

1. $C^{18}O$ *core 10 (adjacent to Tr 14)*.—The integrated intensities of CO ($J = 4-3$) and CO ($J = 1-0$) are the strongest in the observed region, although the integrated intensity of $C^{18}O$ ($J = 1-0$) shows only moderate values. A possible explanation for this is a high excitation temperature due to the star cluster Tr 14: because of the high excitation temperature, the optical depth of $C^{18}O$ ($J = 1-0$) remains very small in spite of its large column density, resulting in very low intensity in $C^{18}O$ ($J = 1-0$)

emission. The NANTEN data indicate the excitation temperature is $\sim$25 K, and this value seems to be a lower limit, since higher resolution data obtained with a 24″ beam show the excitation temperature to be as high as $\sim$45 K (Brooks 2000).

2. $C^{18}O$ *core 5*.—The intensity of CO ($J = 4-3$) is very weak, whereas CO and $C^{18}O$ ($J = 1-0$) emission is quite strong. In general, two explanations are possible: (1) the temperature is not high enough to excite the $J = 4-3$ emission and/or (2) the density is lower than the typical value traced in CO ($J = 4-3$). However, the excitation temperature derived from the CO ($J = 1-0$) observations at NANTEN is 28 K, the highest value among the $C^{18}O$ cores in the observed region. The number density, 2800 cm^{-3}, is also the highest. Moreover, the detection of $H^{13}CO^+$ ($J = 1-0$) emission toward the core indicates that a high-density region of $>10^4$ cm^{-3} exists within the core. Thus, the above two hypotheses fail to explain the properties of the core. High-resolution observations of both low-J and mid-J CO lines may unveil the properties of the core.

4.3. *Characteristics of the Star Formation in the η Car GMC*

In this subsection, we describe the characteristics of the star formation in the η Car GMC. The proportion of massive star–forming cores, i.e., cores with *IRAS* point sources with $L > 10^3\ L_\odot$, 13% (=2/15), is much lower than in massive star–forming regions at distances within a factor of 2 of the η Car GMC: 28% in S35/S37 and 86% in Centaurus III (Saito et al. 1999, 2001). This is consistent with the fact that the ratio of $M_{\rm vir}/M$ is large (see § 3.2); i.e., most of the cores are not gravitationally bound. The large line widths of the cores ($\sim$3 km s^{-1}) compared to those of the other GMCs ($\sim$2 km s^{-1}; see § 3.2) also support this. A large amount of turbulence in the η Car GMC may prevent star formation at the present time.

Let us then consider the origin of the large turbulence in the η Car GMC. The kinetic energy due to the turbulence is roughly estimated from $E_{\rm kin} = \frac{1}{2}MV_{\rm turb}^2$. By using the ^{12}CO mass $M = 3.5\times10^5\ M_\odot$ and the average line width of the $C^{18}O$ cores $V_{\rm turb} = 3$ km s^{-1}, $E_{\rm kin} \sim 3.4\times10^{49}$ ergs is obtained as the kinematic energy of the η Car GMC. The momentum $P = MV_{\rm turb}$ is estimated to be $1.0\times10^6\ M_\odot$ km s^{-1}. In the absence of any mechanisms to prevent it, the turbulence would dissipate on the crossing timescale of the cloud, $t_{\rm cr} \sim R_{\rm cloud}/\Delta V_{\rm cloud}$ (see Vázquez-Semadeni et al. 2000 for a review), which corresponds to $\sim$15 Myr in the case of the η Car GMC. Thus, the presence of a large amount of turbulence means either that the turbulence is somewhat constantly injected by some mechanism or that a large amount of turbulence is still retained although the turbulence is dissipating because the GMC is young and/or the initial amount of turbulence is large. In the following, we examine four possibilities: turbulence injection by (1) mass outflows from young stellar objects, (2) supernova remnants, or (3) stellar winds from massive stars; and (4) the turbulence is preexisting.

1. *Turbulence injection by mass outflows from young stellar objects*.—The kinetic energy and the momentum of such outflows are in the ranges $E = 10^{43}-10^{47}$ ergs and $P = 0.1-1000\ M_\odot$ km s^{-1}, respectively (Fukui et al. 1993). Thus, even if we assume that all outflows have $E = 10^{47}$ ergs and $P = 1000\ M_\odot$ km s^{-1} and that all the energy and momentum of such outflows are converted into turbulence (i.e., conversion coefficient $\epsilon = 1$), at least 1000 YSOs are needed to supply the present turbulence of the η Car GMC.

Here we estimate the contribution of outflows from low-mass YSOs, since most of the stars are formed as clusters in massive star–forming regions. Observationally, it is known that the kinetic energy and the momentum of outflows are correlated with the bolometric luminosity of the driving source, $L_{\rm bol}$ (Wu et al. 2004). Least-squares fits to their data yield $P = 10^{-0.48}L_{\rm bol}^{0.59}$ and $E = 10^{-1.87}L_{\rm bol}^{0.68}$. If we assume that the relation between the mass and the luminosity of YSOs is $L = M^a$ with $a = 3.45$ (Allen 1973) and that the initial mass function (IMF) of YSOs is Scalo's IMF ($dn/dM = M^{-b}$, $b = 2.7$; Scalo 1986) with the cutoff at 1 $M_\odot$, 1.6×10^5 YSOs are needed to supply the present turbulence of the η Car GMC. The number of YSOs largely depends on the cutoff mass of the IMF and the indices a and b; however, 3×10^3 are still needed for the IMF with the cutoff at 3 $M_\odot$ with $a = 4$ and $b = 2$. Although these estimates are quite rough, the number required to supply the present turbulence of the η Car GMC is extremely large compared to the number of YSOs formed in a single GMC under any assumption. Therefore, we can conclude that the turbulence injection by mass outflows from YSOs is not important.

2. *Turbulence injection by supernova remnants*.—The kinetic energy and the initial speed of ejecta of a single supernova remnant are typically $E_{\rm kin} = 10^{51}$ ergs and $V = 10^4$ km s^{-1}, respectively. If we assume the mass of the ejecta to be $M = 3\ M_\odot$, $P = 3\times10^4\ M_\odot$ km s^{-1} can be provided by a single supernova. Thus, even if we assume $\epsilon \sim 1$, at least $\sim$30 supernovae are needed to supply the present turbulence of the η Car GMC, which is too large when we consider the ages of the associated clusters, 3–7 Myr (e.g., Feinstein 1995). The fact that no supernova remnants are known to exist (Whiteoak 1994) supports this, although possible nonthermal radio emission is reported (Jones 1973; Tateyama et al. 1991). Fukui et al. (1999) suggested the possible influence of the Carina flare supershell, which may have been formed by more than 20 supernovae located 100 pc away from the η Car GMC. The momentum supplied to the η Car GMC from the Carina flare supershell through the cross section of the η Car GMC is estimated in the following manner: the total momentum of the Carina flare supershell is assumed to be 20 times the typical momentum of a single supernova. We also assume the depth of the GMC to be the same as the projected extent of the GMC, $\sim$130 pc. The momentum supplied through the cross section of the η Car GMC is estimated to be $P = 3\times10^4\times20\times(130\times130)/(4\pi\times100^2) = 8\times10^4\ M_\odot$ km s^{-1} on the assumption of $\epsilon = 1$, and thus it fails to explain the origin of the turbulence.

3. *Turbulence injection by stellar winds from massive stars*.—The terminal velocity of the stellar wind and the mass-loss rate from η Car are $V = 700$ km s^{-1} and $\dot{M} = 5\times10^{-4}\ M_\odot$ yr^{-1}, respectively (van Boekel et al. 2003; Smith et al. 2003). During the timescale of 10^6 yr, η Car will be able to provide $E_{\rm kin} = 2\times10^{51}$ ergs and $P = 3\times10^5\ M_\odot$ km s^{-1}, which is comparable to the energy and momentum needed if the conversion efficiency is $\sim$100%. However, the effect of the stellar wind will be confined to a small region around η Car; a radius of $\sim$25 pc is derived from the models of Castor et al. (1975) and Weaver et al. (1977) by taking the typical density of a molecular cloud, 100 cm^{-3}, and thus injection from η Car alone is not sufficient to explain the observed turbulence.

There are seven W-R stars and $\sim$80 O-type stars around the η Car GMC (see Fig. 2). Typical values of the terminal velocity of the stellar wind and the mass-loss rate of a W-R star are $V \sim 2000$ km s^{-1} and $\dot{M} = 4\times10^{-5}\ M_\odot$ yr^{-1}, respectively (van der Hucht 2001). The total energy and momentum from these W-R stars in 10^6 yr are estimated to be $E_{\rm kin} = 1.1\times10^{52}$ ergs and $P = 6\times10^5\ M_\odot$ km s^{-1}, respectively. For an O-type star, typical values are $V \sim 1500-2500$ km s^{-1} and $\dot{M} \sim 10^{-5}$ to $10^{-7}\ M_\odot$ yr^{-1} (e.g., Markova et al. 2004). Over a timescale of 10^6 yr, one

O-type star will be able to provide $E_{\rm kin} \sim 2.3 \times 10^{48}$ to 6.3×10^{50} ergs and $P \sim 1.5 \times 10^{2}$ to 2.5×10^{4} $M_{\odot}$ km s^{-1}. Thus, $\sim$100 O stars can provide enough $E_{\rm kin}$ and P on the assumption of $\epsilon = 1$. It may therefore be possible that somewhat uniformly distributed W-R stars and O-type stars account for the large turbulence, although the estimate of ϵ is highly uncertain.

4. *Turbulence is preexisting.*—Bertoldi & McKee (1992) argued that massive cores are magnetically supercritical. This conclusion is extended to low-mass cores by Nakano (1998). Magnetically supercritical cores are supported by turbulence against the pressure of the surrounding medium P_s. When P_s exceeds a critical value $P_{\rm cr}$, the core cannot be in magnetohydrostatic equilibrium and collapses. Nakano (1998) suggested that dissipation of turbulence is the most important process in reducing $P_{\rm cr}$. The condition $P_{\rm cr} < P_s$ can, however, be achieved without dissipating turbulence if P_s is large. Thus, star formation in molecular clouds with large turbulence is possible. Here we investigate the possibility that the η Car GMC still retains a large amount of turbulence although that turbulence is dissipating; i.e., the η Car GMC is not a relaxed system. There are two possibilities: the η Car GMC is young and/or it has an initially large turbulence. The former may be inconsistent with the fact that the ages of the associated clusters are not extremely small, 3–7 Myr (e.g., Feinstein 1995), and thus we concentrate on the latter possibility.

Concerning molecular cloud formation, various theories have been proposed so far: cloud formation by spontaneous instabilities, by the compression of diffuse interstellar medium, and by random coalescence of existing clouds (see Elmegreen 1993 for a review). The most realistic scenario may be a combination of the above processes. The origin of the turbulence in molecular clouds is not yet understood, but possible formation mechanisms of a molecular cloud with large turbulence have been proposed: for example, Koyama & Inutsuka (2000) investigated the propagation of a shock wave into the interstellar medium and suggested that the postshock region collapses into a cold layer through thermal instability. Their recent two-dimensional calculation shows that the layer breaks up into small cloudlets, in which a large amount of molecules are formed in several Myr, and that the velocity dispersion of the cloudlets is typically several km s^{-1} (Koyama & Inutsuka 2002). The fragments then coalesce and become larger clouds with supersonic velocity dispersions. In the case of the η Car GMC, multiple supernova explosions may have contributed to a certain degree; Fukui et al. (1999) suggested that $\sim$20 supernova explosions may have occurred $\sim$100 pc away from the η Car GMC over the last 2×10^{7} yr. These supernova explosions may have triggered the formation of the η Car GMC, as well as the formation of massive stars within the GMC.

Although the above estimate is quite rough, we suggest the possibility that a large amount of turbulence was supplied when the GMC was formed, and it is now dissipating. Identifying the formation mechanism for the η Car GMC is beyond the scope of this paper, but compression due to supernova explosions in the Carina flare supershell may have played an important role. Turbulent injection from stellar winds, supernova remnants, and outflows originating in the stars formed within the GMC may also contribute, supplying turbulence to some degree.

5. SUMMARY

We carried out an unbiased survey for massive dense cores in the giant molecular cloud associated with η Carinae with the NANTEN telescope in the ^{12}CO, ^{13}CO, and C^{18}O $J = 1-0$ emission lines. The purpose of the present study is to obtain a sample of massive *starless* core candidates that are possible sites for future massive star formation. With moderate spatial resolution (2.′7), our observations covered the entire η Car GMC (3×2 deg^2), including regions farther from η Car, where no previous observations had been made except coarse large-scale surveys. We also made high-resolution observations in H^{13}CO$^+$ ($J = 1-0$) with the Mopra 22 m millimeter telescope and searched for molecular outflows in ^{12}CO ($J = 2-1$) toward selected regions with the ASTE 10 m submillimeter telescope. The main results are summarized as follows:

1. We identified 15 C^{18}O cores, whose typical line width $\Delta V_{\rm comp}$, radius r, mass M, column density $N({\rm H_2})$, and average number density $n({\rm H_2})$ were 3.3 km s^{-1}, 2.2 pc, 2.6×10^{3} $M_{\odot}$, 1.3×10^{22} cm^{-2}, and 1.2×10^{3} cm^{-3}, respectively.

2. Two of the 15 cores are associated with *IRAS* point sources whose luminosities are larger than 10^4 $L_{\odot}$, which indicates that massive star formation is occurring within these cores. Five cores, including the two with *IRAS* sources, are associated with *MSX* point sources. We detected H^{13}CO$^+$ ($J = 1-0$) emission toward four C^{18}O cores, of which two are associated with *IRAS* and *MSX* point sources, another one is associated only with an *MSX* point source, and the other is associated with neither *IRAS* nor *MSX* point sources. The core with neither *IRAS* nor *MSX* point sources shows the presence of a bipolar molecular outflow in ^{12}CO ($J = 2-1$), which indicates that star formation is also occurring in the core, and the other three of the four H^{13}CO$^+$ detections show winglike emission. In total, six C^{18}O cores out of 15 (=40%) have experienced star formation, and at least 2 of15 (=13%) are massive star–forming cores in the η Car GMC.

3. We found that massive star formation occurs preferentially in cores with larger $N({\rm H_2})$, M, and $n({\rm H_2})$ and a smaller ratio of $M_{\rm vir}/M$. We also found that the cores in the η Car GMC are characterized by large ΔV and $M_{\rm vir}/M$ on average compared to the cores in other GMCs observed with the same telescope. These properties of the cores may account for the fact that as much as 60%–87% of the cores do not show any signs of massive star formation.

4. We investigated the origin of a large amount of turbulence in the η Car GMC. We found that turbulence injection from stellar winds, molecular outflows, and supernova remnants that originated from stars formed within the GMC is not enough to explain the existing turbulence. We propose the possibility that the large turbulence was preexisting when the GMC was formed and is now dissipating. Mechanisms such as multiple supernova explosions in the Carina flare supershell may have contributed to form a GMC with a large amount of turbulence.

The NANTEN project (southern 4 m radio telescope) is based on a mutual agreement between Nagoya University and the Carnegie Institution of Washington. We greatly appreciate the hospitality of all staff members of the Las Campanas Observatory of the Carnegie Institution of Washington. We also acknowledge that the realization of this project was made possible by contributions from many Japanese public donors and companies. ASTE (Atacama Submillimeter Telescope Experiment) is a joint project between Japan and Chile. The telescope is operated by the ASTE team, including NAOJ, University of Tokyo, Nagoya University, Osaka Prefecture University, and Universidad de Chile. We are grateful to all the members of the ASTE team. We are grateful to the ATNF for their hospitality and to the staff of Mopra Observatory, especially Stuart Robertson for

his help with the observations. The Australia Telescope is funded by the Commonwealth of Australia for operation as a National Facility managed by CSIRO. This work made use of the Southern Hα Sky Survey Atlas (SHASSA), which is supported by the National Science Foundation. The Digitized Sky Surveys were produced at the Space Telescope Science Institute under US Government grant NAGW-2166. The images of these surveys are based on photographic data obtained using the Oschin Schmidt Telescope on Palomar Mountain and the UK Schmidt Telescope. The plates were processed into the present compressed digital form with the permission of these institutions. We are also grateful to Akiko Kawamura, Yoshiaki Moriguchi, Masanori Nakagawa, and Joanne Dawson for their helpful comments. This work was financially supported in part by Grants-in-Aid for Scientific Research (KAKENHI) from the Ministry of Education, Culture, Sports, Science, and Technology of Japan (MEXT) and the Japan Society for the Promotion of Science (JSPS), Nos. 14102003, 14403001, 15071202, and 15071205.

REFERENCES

Allen, C. W. 1973, Astrophysical Quantities (London: Athlone)
Alves, J., & Homeier, N. 2003, ApJ, 589, L45
André, P., Ward-Thompson, D., & Barsony, M. 1993, ApJ, 406, 122
Aoyama, H., Mizuno, N., Yamamoto, H., Onishi, T., Mizuno, A., & Fukui, Y. 2001, PASJ, 53, 1053
Bergin, E. A., Goldsmith, P. F., Snell, R. L., & Langer, W. D. 1997, ApJ, 482, 285
Bertoldi, F., & McKee, C. F. 1992, ApJ, 395, 140
Bertsch, D. L., Dame, T. M., Fichtel, C. E., Hunter, S. D., Sreekumar, P., Stacy, J. G., & Thaddeus, P. 1993, ApJ, 416, 587
Beuther, H., Schilke, P., Menten, K. M., Motte, F., Sridharan, T. K., & Wyrowski, F. 2002a, ApJ, 566, 945
Beuther, H., Schilke, P., Sridharan, T. K., Menten, K. M., Walmsley, C. M., & Wyrowski, F. 2002b, A&A, 383, 892
Bloemen, J. B. G. M., et al. 1986, A&A, 154, 25
Bonnell, I. A., Bate, M. R., & Zinnecker, H. 1998, MNRAS, 298, 93
Brooks, K. 2000, Ph.D. thesis, Univ. New South Wales
Brooks, K. J., Cox, P., Schneider, N., Storey, J. W. V., Poglitsch, A., Geis, N., & Bronfman, L. 2003, A&A, 412, 751
Brooks, K. J., Whiteoak, J. B., & Storey, J. W. V. 1998, Publ. Astron. Soc. Australia, 15, 202
Cabrit, S., & Bertout, C. 1992, A&A, 261, 274
Caselli, P., & Myers, P. C. 1995, ApJ, 446, 665
Castor, J., McCray, R., & Weaver, R. 1975, ApJ, 200, L107
Cox, P., & Bronfman, L. 1995, A&A, 299, 583
Davidson, K., & Humphreys, R. M. 1997, ARA&A, 35, 1
de Graauw, T., Lidholm, S., Fitton, B., Beckman, J., Israel, F. P., Nieuwenhuijzen, H., & Vermue, J. 1981, A&A, 102, 257
Dickman, R. L. 1978, ApJS, 37, 407
Dobashi, K., Bernard, J. P., & Fukui, Y. 1996, ApJ, 466, 282
Dobashi, K., Bernard, J. P., Yonekura, Y., & Fukui, Y. 1994, ApJS, 95, 419
Elmegreen, B. G. 1993, in Protostars and Planets III, ed. E. H. Levy & J. I. Lunine (Tucson: Univ. Arizona Press), 97
Evans, N. J., II. 1999, ARA&A, 37, 311
Evans, N. J., II, Shirley, Y. L., Mueller, K. E., & Knez, C. 2002, in ASP Conf. Ser. 267, The Earliest Stages of Massive Star Birth, ed. P. A. Crowther (San Francisco: ASP), 17
Ezawa, H., Kawabe, R., Kohno, K., & Yamamoto, S. 2004, Proc. SPIE, 5489, 763
Faúndez, S., Bronfman, L., Garay, G., Chini, R., Nyman, L. Å., & May, J. 2004, A&A, 426, 97
Feinstein, A. 1995, Rev. Mex. AA, 2, 57
Forbrich, J., Schreyer, K., Posselt, B., Klein, R., & Henning, Th. 2004, ApJ, 602, 843
Frerking, M. A., Langer, W. D., & Wilson, R. W. 1982, ApJ, 262, 590
Fukui, Y. 1989, in Proc. ESO Workshop on Low Mass Star Formation and Pre–Main Sequence Objects, ed. B. Reipurth (ESO: Garching), 95
Fukui, Y., Iwata, T., Mizuno, A., Bally, J., & Lane, A. P. 1993, in Protostars and Planets III, ed. E. H. Levy & J. I. Lunine (Tucson: Univ. Arizona Press), 603
Fukui, Y., Ogawa, H., Kawabata, K., Mizuno, A., & Sugitani, K. 1991, in IAU Symp. 148, The Magellanic Clouds, ed. R. Haynes & D. Milne (Dordrecht: Kluwer), 105
Fukui, Y., Onishi, T., Abe, R., Kawamura, A., Tachihara, K., Yamaguchi, R., Mizuno, A., & Ogawa, H. 1999, PASJ, 51, 751
Fukui, Y., & Sakakibara, O. 1992, Mitsubishi Electric Adv., 60, 11
Fukui, Y., Sugitani, K., Takaba, H., Iwata, T., Mizuno, A., Ogawa, H., & Kawabata, K. 1986, ApJ, 311, L85
Fukui, Y., & Yonekura, Y. 1998, in IAU Symp. 179, New Horizons from Multi-Wavelength Sky Surveys, ed. B. J. McLean et al. (Dordrecht: Kluwer), 165
Garay, G., Faúndez, S., Mardones, D., Bronfman, L., Chini, R., & Nyman, L.-Å. 2004, ApJ, 610, 313
Gaustad, J. E., McCullough, P. R., Rosing, W., & Van Buren, D. 2001, PASP, 113, 1326
Goldsmith, P. F., & Langer, W. D. 1978, ApJ, 222, 881
Goodman, A. A., Barranco, J. A., Wilner, D. J., & Heyer, M. H. 1998, ApJ, 504, 223
Grabelsky, D. A., Cohen, R. S., Bronfman, L., & Thaddeus, P. 1988, ApJ, 331, 181
Grabelsky, D. A., Cohen, R. S., Bronfman, L., Thaddeus, P., & May, J. 1987, ApJ, 315, 122
Hara, A., Tachihara, K., Mizuno, A., Onishi, T., Kawamura, A., Obayashi, A., & Fukui, Y. 1999, PASJ, 51, 895
Harju, J., Walmsley, C. M., & Wouterloot, J. G. A. 1993, A&AS, 98, 51
Hunter, S. D., et al. 1997, ApJ, 481, 205
Jijina, J., Myers, P. C., & Adams, F. C. 1999, ApJS, 125, 161
Johansson, L. E. B., et al. 1984, A&A, 130, 227
Jones, B. B. 1973, Australian J. Phys., 26, 545
Jørgensen, J. K., Schöier, F. L., & van Dishoeck, E. F. 2004, A&A, 416, 603
Kato, S., Mizuno, N., Asayama, S., Mizuno, A., Ogawa, H., & Fukui, Y. 1999, PASJ, 51, 883
Kawamura, A., Onishi, T., Yonekura, Y., Dobashi, K., Mizuno, A., Ogawa, H., & Fukui, Y. 1998, ApJS, 117, 387
Kim, B. G., Kawamura, A., Yonekura, Y., & Fukui, Y. 2004, PASJ, 56, 313
Kohno, K., et al. 2004, in The Dense Interstellar Medium in Galaxies, ed. S. Pfalzner et al. (Berlin: Springer), 349
Koyama, H., & Inutsuka, S. 2000, ApJ, 532, 980
———. 2002, ApJ, 564, L97
Kurtz, S., Cesaroni, R., Churchwell, E., Hofner, P., & Walmsley, C. M. 2000, in Protostars and Planets IV, ed. V. Mannings, A. Boss, & S. Russell (Tucson: Univ. Arizona Press), 299
Kutner, M. L., & Ulich, B. L. 1981, ApJ, 250, 341
Lada, C. J. 1985, ARA&A, 23, 267
Lada, E. A., Bally, J., & Stark, A. A. 1991, ApJ, 368, 432
Ladd, E. F., Myers, P. C., & Goodman, A. A. 1994, ApJ, 433, 117
Ladd, N., Purcell, C., Wong, T., & Robertson, S. 2005, Publ. Astron. Soc. Australia, 22, 62
Levreault, R. M. 1988, ApJS, 67, 283
Maíz-Apellániz, J., Walborn, N. R., Galué, H. Á., & Wei, L. H. 2004, ApJS, 151, 103
Markova, N., Puls, J., Repolust, T., & Markov, H. 2004, A&A, 413, 693
McKee, C. F., & Tan, J. C. 2003, ApJ, 585, 850
Megeath, S. T., Cox, P., Bronfman, L., & Roelfsema, P. R. 1996, A&A, 305, 296
Mizuno, A., Onishi, T., Hayashi, M., Ohashi, N., Sunada, K., Hasegawa, T., & Fukui, Y. 1994, Nature, 368, 719
Mizuno, A., Onishi, T., Yonekura, Y., Nagahama, T., Ogawa, H., & Fukui, Y. 1995, ApJ, 445, L161
Mizuno, A., et al. 1998, ApJ, 507, L83
———. 1999, PASJ, 51, 859
Mueller, K. E., Shirley, Y. L., Evans, N. J., II, & Jacobson, H. R. 2002, ApJS, 143, 469
Myers, P. C., Ladd, E. F., & Fuller, G. A. 1991, ApJ, 372, L95
Nagahama, T. 1997, Ph.D. thesis, Nagoya Univ.
Nakano, T. 1998, ApJ, 494, 587
Nozawa, S., Mizuno, A., Teshima, Y., Ogawa, H., & Fukui, Y. 1991, ApJS, 77, 647
Obayashi, A., Kun, M., Sato, F., Yonekura, Y., & Fukui, Y. 1998, AJ, 115, 274
Ogawa, H., Mizuno, A., Hoko, H., Ishikawa, H., & Fukui, Y. 1990, Int. J. Infrared Millimeter Waves, 11, 717
Onishi, T., Mizuno, A., Kawamura, A., Ogawa, H., & Fukui, Y. 1996, ApJ, 465, 815
———. 1998, ApJ, 502, 296
Onishi, T., Mizuno, A., Kawamura, A., Tachihara, K., & Fukui, Y. 2002, ApJ, 575, 950
Onishi, T., et al. 1999, PASJ, 51, 871
Rathborne, J. M., Brooks, K. J., Burton, M. G., Cohen, M., & Bontemps, S. 2004, A&A, 418, 563

Saito, H., Mizuno, N., Moriguchi, Y., Matsunaga, K., Onishi, T., Mizuno, A., & Fukui, Y. 2001, PASJ, 53, 1037
Saito, H., Tachihara, K., Onishi, T., Yamaguchi, N., Mizuno, N., Mizuno, A., Ogawa, H., & Fukui, Y. 1999, PASJ, 51, 819
Scalo, J. M. 1986, Fundam. Cosmic Phys., 11, 1
Sekimoto, Y., et al. 2001, PASJ, 53, 951
Shepherd, D. S., & Churchwell, E. 1996, ApJ, 472, 225
Shirley, Y. L., Evans, N. J., II, Young, K. E., Knez, C., & Jaffe, D. T. 2003, ApJS, 149, 375
Shu, F. H., Adams, F. C., & Lizano, S. 1987, ARA&A, 25, 23
Smith, N., Davidson, K., Gull, T. R., Ishibashi, K., & Hillier, D. J. 2003, ApJ, 586, 432
Smith, N., Egan, M. P., Carey, S., Price, S. D., Morse, J. A., & Price, P. A. 2000, ApJ, 532, L145
Solomon, P. M., Rivolo, A. R., Barrett, J., & Yahil, A. 1987, ApJ, 319, 730
Sorai, K., Sunada, K., Okumura, S. K., Iwasa, T., Tanaka, A., Natori, N., & Onuki, H. 2000, Proc. SPIE, 4015, 86
Sridharan, T. K., Beuther, H., Schilke, P., Menten, K. M., & Wyrowski, F. 2002, ApJ, 566, 931
Stacy, J. G., Benson, P. J., Myers, P. C., & Goodman, A. A. 1988, in Interstellar Matter: Proc. 2nd Haystack Obs. Meeting, ed. J. M. Moran & P. T. P. Ho (New York: Gordon & Breach), 179
Strong, A. W., et al. 1988, A&A, 207, 1
Sutton, E. C., Blake, G. A., Masson, C. R., & Phillips, T. G. 1985, ApJS, 58, 341
Tachihara, K., Mizuno, A., & Fukui, Y. 2000, ApJ, 528, 817
Tachihara, K., Onishi, T., Mizuno, A., & Fukui, Y. 2002, A&A, 385, 909
Tateyama, C. E., Strauss, F. M., & Kaufmann, P. 1991, MNRAS, 249, 716
Ulich, B. L., & Haas, R. W. 1976, ApJS, 30, 247
van Boekel, R., et al. 2003, A&A, 410, L37
van der Hucht, K. A. 2001, NewA Rev., 45, 135
Vázquez-Semadeni, E., Ostriker, E. C., Passot, T., Gammie, C. F., & Stone, J. M. 2000, in Protostars and Planets IV, ed. V. Mannings, A. Boss, & S. Russell (Tucson: Univ. Arizona Press), 3
Warin, S., Benayoun, J. J., & Viala, Y. P. 1996, A&A, 308, 535
Weaver, R., McCray, R., Castor, J., Shapiro, P., & Moore, R. 1977, ApJ, 218, 377
Whiteoak, J. B. Z. 1994, ApJ, 429, 225
Wouterloot, J. G. A., Walmsley, C. M., & Henkel, C. 1988, A&A, 203, 367
Wu, Y., Wei, Y., Zhao, M., Shi, Y., Yu, W., Qin, S., & Huang, M. 2004, A&A, 426, 503
Yamaguchi, N., Mizuno, N., Saito, H., Matsunaga, K., Mizuno, A., Ogawa, H., & Fukui, Y. 1999a, PASJ, 51, 775
Yamaguchi, R., Saito, H., Mizuno, N., Mine, Y., Mizuno, A., Ogawa, H., & Fukui, Y. 1999b, PASJ, 51, 791
Yonekura, Y., Dobashi, K., Hayashi, Y., Sato, F., Ogawa, H., & Fukui, Y. 1998, AJ, 115, 2009
Yonekura, Y., Dobashi, K., Mizuno, A., Ogawa, H., & Fukui, Y. 1997, ApJS, 110, 21
Yonekura, Y., Mizuno, N., Saito, H., Mizuno, A., Ogawa, H., & Fukui, Y. 1999, PASJ, 51, 911
Yu, Z.-A., Nagahama, T., & Fukui, Y. 1996, ApJ, 471, 867
Zhang, Q., Hunter, T. R., Brand, J., Sridharan, T. K., Molinari, S., Kramer, M. A., & Cesaroni, R. 2001a, ApJ, 552, L167
Zhang, X., Lee, Y., Bolatto, A., & Stark, A. A. 2001b, ApJ, 553, 274